# GeoDIN — Geoscience-Based Deep Interaction Networks for Predicting Flow Dynamics in Reservoir Simulation Models

*Dr. Marko Maucec and Ridwan S. Jalali*

**Abstract /**

Network graphs represent a general language for describing complex systems and a framework for knowledge discovery. Graph learning is a new concept with applications emerging in biomedicine, pharmacology, smart mobility, and physical reasoning. When applied to petroleum systems, such as reservoir models, graphs provide unique differentiators for the abstraction of reservoir connectivity to facilitate "reservoir centric" machine learning applications.

In this article, we demonstrate, for the first time, the application of Geoscience-based Deep Interaction Networks (GeoDIN) to learn complex physics relationships from 3D reservoir models for fast and accurate prediction of subsurface spatiotemporal flow dynamics. We build the network graph with embedded subsurface and physics representations and train the machine learning model to "act like the reservoir simulator."

We use a simulation benchmark model for two-phase incompressible flow, with an approximate 1.1 million grid size, one central injector and four corner producers. Static 3D grid properties include porosity and permeability. We use a full physics simulation output to construct the interaction network graph, where graph node objects (nodes) represent reservoir grid cells. We embed the feature vector combining pore, oil, and water volumes, pressure, and relative permeability. The graph objects representing wells are connected with well completion factors. The producing wells have embedded oil and water production rates, while the objects representing injecting wells have embedded water injection rates. We represent graph relations (edges) with bidirectional transmissibility of the source cell. To preprocess the data for machine learning, we scale the graph object attributes using "min-max" normalization and we normalize the graph relation attributes using Box-Cox transformation.

We train the GeoDIN framework to predict oil and water saturation dynamics in space and time. When benchmarked with full physics simulation, the interaction networks ran on two V100 GPUs and substantially accelerated the prediction phase compared to a physics-based simulator running on 70 Intel Xeon E5 CPU cores. On average, the error in GeoDIN predicted spatiotemporal distribution of oil saturation remains within 5% of full physics simulation for 90% of the model grid cells, while the error in water saturation remains within 2.5% of full physics simulation.

The spatiotemporal propagation of pressure is more sensitive to local embeddings of interaction networks, which communicate on node-to-node information transfer. This results in a larger prediction error of the GeoDIN model when benchmarked to full physics simulation. On average, the error distribution suggests that a great majority (90% to 95%) of grid cells fall within 10% to 30% error bound, relative to the full physics simulation.

The presented GeoDIN approach to network learning carries a game changing potential for prediction of subsurface flow dynamics. As the way forward, we will investigate implementation of graph neural networks (NN) with automated feature learning, generalization, and scale up.

## Introduction

Accurate numerical simulation of flow dynamics in subsurface reservoir systems lies at the heart of petroleum engineering and science. Reservoir simulation has become a standard tool for hydrocarbon reserve assessment, field development planning, and optimization and for strategic decision making purposes. The state-of-the-art simulation models of mature, real-life hydrocarbon assets can exceed hundreds of millions in grid-size, integrate thousands of wells and span decades of production history under various operational scenarios. Despite the wide expansion and deployment of massively parallelized high performance computing (HPC) clusters, novel GPU-based architectures and cloud computing, advanced reservoir simulation still poses extreme computational challenges to dynamic model calibration and optimization, long-term forecasting, and rigorous uncertainty and risk analysis.

Driven by advances in machine learning and deep learning, alternative approaches to predictive modeling and

simulations of complex petroleum systems' behavior have been proposed in the form of physics informed, referred to as scientific machine learning, or SciML. By incorporating physical knowledge, constraints and conservation laws into machine learning and deep learning, one can potentially reduce the data requirements and dependency, significantly improve the predictive accuracy, statistical efficiency, interpretability and generalizability of the model, eliminate physically implausible predictions from the search space and reduce the computational cost of models[1].

Recently, the amalgamation of data and physics governed machine learning and deep learning modeling in the energy and oil and gas domains has gained significant momentum in research and development. Zhao and Sarma (2018)[2] introduce the data physics technology that combines the reservoir physics with machine learning and benchmark it against the conventional simulator for thermal recovery problems while dramatically reducing the computational run time. Klie et al. (2020)[3] introduce the application of integrated transfer learning from previously learned full physics development scenarios to accelerate and optimize the execution of the forthcoming field development plan.

Zhang et al. (2019)[4] used the deep learning concepts combined with model reduction schemes to predict multiphase flow dynamics, while Jin et al. (2019)[5] and Al-Sulaimani and Wheeler (2021)[6] deploy physics-based reduced order modeling with Embed-to-Control framework[7] for multiphase surface flow simulation. Fraces et al. (2020)[8] used physics informed neural networks (PINN) and apply transfer learning and generative methods to solve an inference problem for two-phase immiscible transport, while Wang et al. (2020)[9], (2021)[10] introduced the concept of the theory guided NNs to incorporate governing equations, boundary conditions and practical experience into multiphase flow prediction.

In another approach, Thavarajah et al. (2021)[11] trained a deep learning-based proxy model by full physics simulation output using the encoder-decoder NNs (convolutional long short-term memory (LSTM)) to simulate fluid dynamics. While Cai et al. (2021)[12] and references therein provide a review of PINNs for solving inverse problems in fluid mechanics, Fuks and Tchelepi (2020)[13] demonstrated that physics informed machine learning approaches fail to approximate the fluid flow dynamics governed by nonlinear partial differential equations (PDEs) in the presence of sharp variations of saturation and propose the solution by adding a small amount of diffusion to the conservation equation.

In our article, we approach the training of the machine learning and deep learning model with subsurface physics and solve the forward predictive problem by encoding the reservoir simulation model as a network graph. Network graphs represent a general language for describing complex systems and a framework for knowledge discovery. Representation learning on graphs is a new concept with applications in biomedicine[14], pharmacology and drug discovery[15], smart mobility[16] and physical reasoning and inference[17]. Recently, the applications of network graph

modeling and learning were introduced for subsurface modeling and optimization[18] using a hybrid artificial intelligence framework, and for learning to simulate complex physical[19] and chemical processes[20].

When applied to reservoir models, graphs provide unique functionality for the abstraction of reservoir connectivity and enable generalization from well centric to reservoir centric machine learning and deep learning applications. We leverage the concept of an interaction network framework[21] and build the network graph with embedded subsurface and physics representations, and train the deep learning model to act like the reservoir simulator.

## Models and Methods

### Reservoir Simulation Model

We use the SPE10[23] as a reference reservoir simulation model. The geological model represents a part of a Brent sequence described on a regular Cartesian grid with $60 \times 220 \times 85$ (1,122,000) cells. The model consists of two formations: a shallow marine Tarbert formation in the top 35 layers, where the permeability is relatively smooth, and a fluvial Upper-Ness permeability in the bottom 50 layers. Both formations are characterized by large permeability variations, with eight to 12 orders of magnitude, but are qualitatively different, Fig. 1. The porosity field is strongly correlated to the permeability, and about 2.5% of the blocks have zero porosity assigned as inactive.

The reservoir is produced using a water drive from a vertical well in the center of the reservoir with a constant injection rate of 5,000 stock tank barrels per day and produced from four vertical wells at the corners, each at a bottom-hole pressure of 4,000 psi. We simulated 1,827 days of production assuming incompressible flow, running on 70 Intel Xeon E5 CPU cores of a highly parallelized HPC cluster.

### Interaction Networks

The concept of modeling an interaction network was introduced[21] to reason how objects in complex dynamic systems interact, to infer the abstract system properties and relations, and to enable dynamical predictions. The

---

**Fig. 1** *The SPE10 reservoir simulation model: 3D model renderings of X-permeability (left) and Z-permeability (right) with a vertical central injector and the four corner producers, completed top to bottom.*
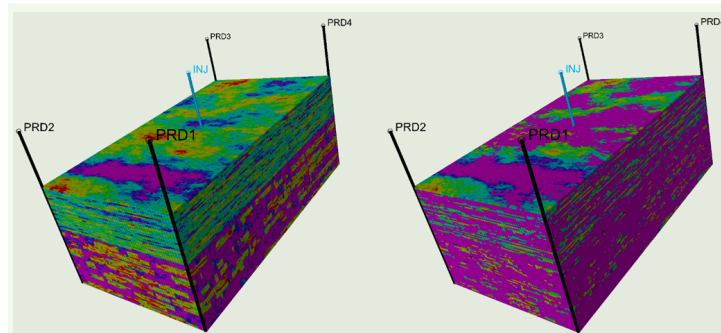
interaction network model represents the first, general purpose, learnable physics engine and was evaluated with experiments in several challenging physical domains: n-body problems, rigid-body collision, and nonrigid dynamics.

In the simplified example to predict the dynamics of a single object, one may use an object centric function, $f_O$, which takes the objects' state, $o_t$, as the input at time, $t$, and outputs the new states of the object, $o_{t+1}$, at future time, $t+1$. Moreover, if the two or more objects are governed by the same dynamics, $f_O$ could be applied independently to predict the future states of such objects.

Consequently, if several objects interact with each other, the $f_O$ is insufficient because it does not capture the inter-object relationships. For example, when the first object, $o_1$, defined as the sender, influences the second object, $o_2$, defined as the receiver via directed interaction, the interaction network model introduces a relation centric function, $f_R$, to predict the effect of this interaction, $e_{t+1}$, on the receiving object $o_2$. The $f_R$ takes as input the objects $o_1$ and $o_2$, as well the properties of their relationship, $r$:

$$e_{t+1} = f_R(o_{1,t}, o_{2,t}, r) \qquad \text{1}$$

The $f_O$ is modified so it can input both, the effect of interaction $e_{t+1}$ caused by $r$ and the current state of the receiving object, $o_{2,t}$, to predict the future (dynamic) state of the receiving object, $o_{2,t+1}$:

$$o_{2,t+1} = f_O(o_{2,t}, e_{t+1}) \qquad \text{2}$$

For larger and more complex systems, Battaglia et al. (2016)[21] generalizes Eqn. 2 by introducing the model input in the form of a graph, $G = \langle O, R \rangle$[21]. They assume an attributed, directed multigraph as the relations have attributes and there can be multiple distinct relations between two objects. For a system with $N_O$ objects and $N_R$ relations, Battaglia et al. (2016)[21] defines the inputs to the interaction network as $O = \{o_j\}_{j=1\ldots N_O}$, $R = \{\langle i, j, r_k \rangle_k\}_{k=1\ldots N_R}$ where $i \neq j, 1 \leq i, j \leq N_O$ and $X = \{x_j\}_{j=1\ldots N_O}$. The $O$ represents the states of each object while the triplet $\langle i, j, r_k \rangle_k$ represents the $k$-th relation in the system, from sender $o_i$, to receiver $o_j$, with relation attribute, $r_k$. The $X$ represents the external effects, such as active control inputs or constraints that manipulate objects and can be applied to each object separately. The basic interaction network is defined as:

$$IN(G) = \emptyset_O(a(G, X, \emptyset_R(m(G)))) \qquad \text{3}$$

where

$$m(G) = B = \{b_k\}_{k=1\ldots N_R} \qquad a(G, X, E) = C = \{c_j\}_{j=1\ldots N_O}$$

$$f_R(b_k) = e_k \qquad f_O(c_j) = p_j$$

$$\emptyset_R(B) = E = \{e_k\}_{k=1\ldots N_R} \qquad \emptyset_O(C) = P = \{p_j\}_{j=1\ldots N_O} \qquad \text{4}$$

The marshalling function $m$, rearranges the objects and relations into pair-wise interaction terms and compute their effects, $e_k$, via relational model, $\Phi_R$, using the relation centric function, $f_R(\cdot)$. The aggregation function $a$, aggregates the $e_k$ and combines them with $o_j$ and $x_j$, to generate the input for an object model, $\Phi_O$, using the object-centric function, $f_O(\cdot)$. The $f_O(\cdot)$ predicts how the object's interactions, dynamics, and external effects influence the behavior of objects. This basic interaction network can predict the evolution of the states in a dynamic system, and for physical simulation, $P$ may equal to the future (predicted) states of the objects, $O_{t+1}$. For further details on mathematical frameworks and notations related to interaction network modeling, refer to Battaglia et al. (2016)[21].

## Geoscience-Based Deep Interaction Networks (GeoDIN)

The concept of an interaction network is … agnostic to the choice of functions and algorithms …, for a learnable implementation capable of reasoning about complex systems with nonlinear relations and dynamics[21]. In our work, we formalize and expand the implementation to the domain of petroleum systems and develop Geoscience-based Deep Interaction Networks (GeoDIN) to predict complex fluid-flow dynamics in reservoir simulation models. In Fig. 2, we partially reproduce Fig. 1 from Battaglia et al. (2016)[21] to schematize the architecture of the GeoDIN with an annotated forward calculation.

**Data Abstraction:** We parse the output of the simulation run from an in-house, full physics, massively parallelized reservoir simulator[24]. The data format of the simulation output is a customized format for reading and writing the result files from the Eclipse reservoir simulator[25]. We build a network graph with object/node and relation/edge attributes and types, Table 1. To preprocess the data for machine learning, we scale the graph object attributes using "min-max" normalization and we normalize the graph relation attributes, i.e., cell transmissibility ($TRANS$), using Box-Cox transformation. Relation/edge types were one-hot encoded into a vector of size 3.

In Fig. 3, we show examples of network graph representations for the reservoir simulation grid, Nx = 3, Ny = 3, Nz = 1 (left), and Nx = 10, Ny = 10, Nz = 3 (right), where graph edges are color-coded with source $TRANS$ and graph nodes are color-coded with cell oil saturation, $SOIL$.

The dimensionality of the relations vector (the number of graph edges, $N_R$) is a dynamic, simulation case dependent variable: as indicated in Fig. 3, the $3 \times 3 \times 1$ simulation grid (with only lateral grid communication via x- and y-transmissibility) results in a graph representation with 24 relations/edges. The $10 \times 10 \times 3$ simulation grid on the other hand, renders 1,480 relations/edges that account for both, the lateral and vertical (multilayer) grid communication, embedded with full, 3D transmissibility tensor. The network graph representations of reservoir simulation grids become significantly more complex when additional abstractions of grid connectivity are integrated, such as sealing faults or fracture networks or models with unstructured grids and the presence of nonneighbor connections.

**Implementation:** We define an array of objects ($O$) as the $N_O \times D_s$ array. The columns correspond to the number

**Fig. 2** *A schematic of a GeoDIN model architecture. The model takes as input a graph that represents a system of objects, $o_j$, in between relations $\langle i, j, r_k \rangle_k$ and external effects, $x_j$. It establishes the pair-wise interaction terms, $b_k$, and computes their effects, $e_k$, via a relational model, $f_R(\cdot)$, represented by the first feedforward neural network (FFNN). The $e_k$ are then aggregated and combined with the $o_j$, to generate input (as $c_j$), for an object model, $f_O(\cdot)$, with a second FFNN, which predicts how the interactions and dynamics influence the objects, p.*
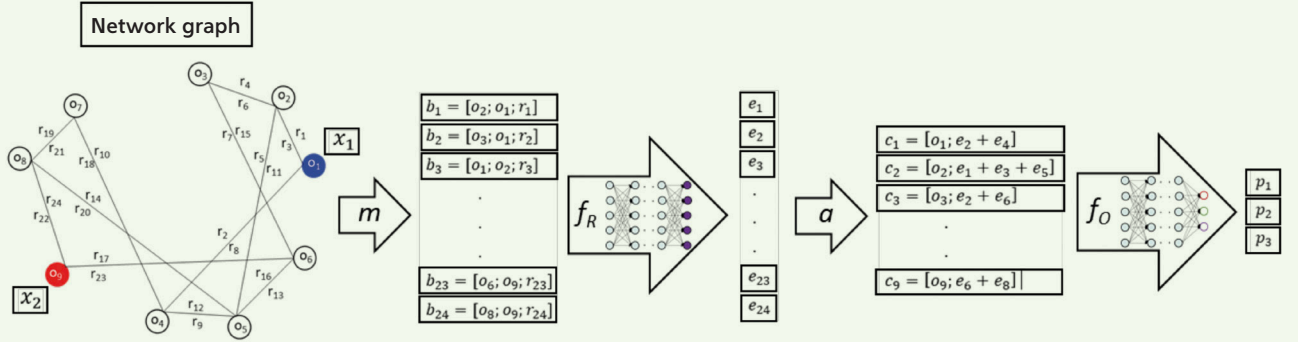


**Table 1** *Features and encodings of a GeoDIN graph.*

| | | | | |
|---|---|---|---|---|
| **Object/Node** (object state variables: $D_S$) | Attribute | Oil saturation | $\boldsymbol{D_{SDyn}}$ | SOIL |
| | | Water saturation | | SWAT |
| | | Pressure | | PRESS |
| | | Pore volume | | PORVOL |
| | | Porosity | | POROS |
| | | Permeability tensor | $\boldsymbol{D_{SStat}}$ | PERM |
| | | Connate water saturation (0.2; constant) | | SWC |
| | | Oil-water relative permeability endpoints | | KRW, KROW |
| | | Oil Production Rate (Producer) | | WOPR |
| | | Water Production Rate (Producer) | $\boldsymbol{X}$ | WWPR |
| | | Water Injection Rate (Injector) | | WWIR |
| **Relation/Edge** (relation variables: $D_R$) | Attribute | Transmissibility tensor of source cell | | TRANS |
| | | Well completion factor | | CF |
| | Type | Simulation Grid Cells | | DIFFUSE |
| | | Producing Wells | | PRODUCE |
| | | Injecting Wells | | INJECT |

of graph objects, $N_O = N_{gc} + N_{pw} + N_{iw}$, where $N_{gc}$, $N_{pw}$, and $N_{iw}$ represent the number of simulation grid cells, the number of producing, and the number of injecting wells, respectively. The rows correspond to the objects' $D_S$ length state vector and $D_S = D_{SDyn} + D_{SStat} + X$. In the GeoDIN model, the elements of the state vector are categorized as:

- Dynamic state variables, $D_{SDyn}$, that combine cell attributes such as *SOIL*, water saturation, *SWAT*, and

reservoir pressure, *PRESS*, subject to a spatiotemporal update in each time step of the GeoDIN prediction.

- Static state variables, $D_{SStat}$, that combine cell attributes like porosity, *POROS*, and permeability, *PERM*, tensors as well as pore volume, *PORVOL*, which was used to constrain the NN while training with simulation data and limit error accumulation in predicted barrels of fluid. The object's model was augmented with relative permeability to capture

**Fig. 3** *The network graph representations for the reservoir simulation grid (3 × 3 × 1; left) and (10 × 10 × 3; right).*
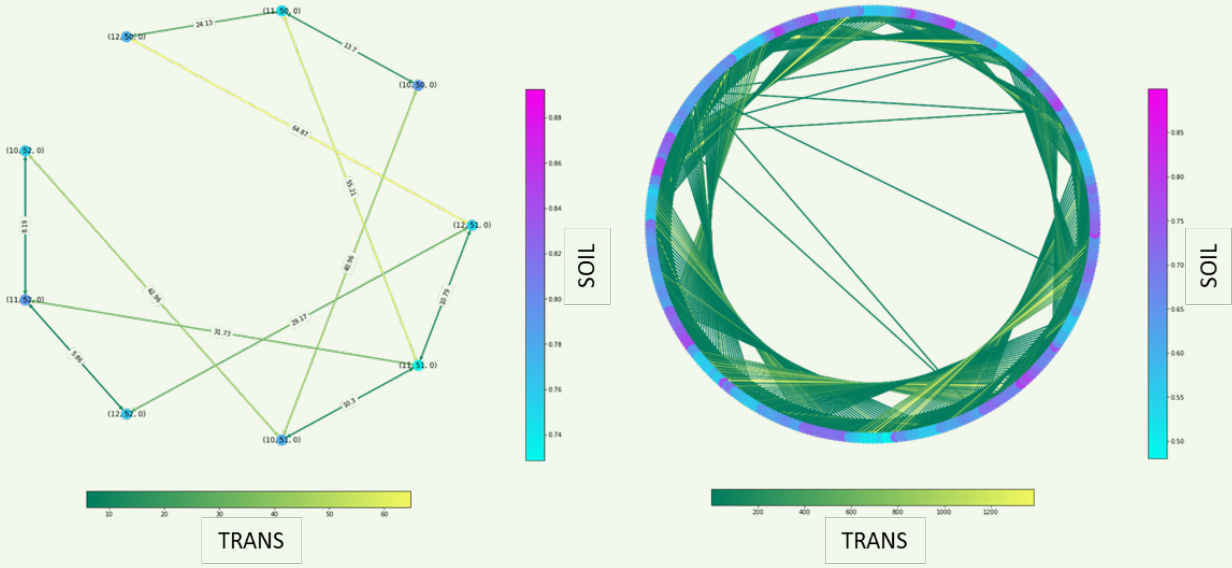


correct two-phase flow dynamics and note-to-node information transfer of spatiotemporal fluid propagation in the training phase. Encoding the relative permeability parameters, i.e., connate water saturation, $SWC$, and oil-water endpoints, $KRW$, $KROW$, as a Corey function, Fig. 4, instead in its tabular form, accelerates the deep NN training.

- Operational state variables, $X$, that combine well attributes such as the oil production rate, $WOPR$, and water production rate, $WWPR$, for producers and water injection rate, $WWIR$, for injectors, encoded as control variables, representing well operational constraints per each time step.

The relations ($R$) are represented as a triplet $R = \langle R_R, R_S, R_I \rangle$, where:

- $R_R$ and $R_S$ are $N_O \times N_g$ arrays, which index the receiver and sender objects, respectively.

- $R_I$ represents the $D_R \times N_R$ array where $D_R$ sums over the number or relation attributes and types. In GeoDIN, we encode two relation types: bidirectional $TRANS$ and well completion factor, CF. Both, the $TRANS$ and CF are continuous variables. The relation type is one-hot encoded into a vector of size 3 with categorical representation of how interacting objects in the triplet $R$ exchange the information ($DIFFUSE$ for grid cell-to-cell communication and $PRODUCE/INJECT$ for well-to-cell communication), which makes $D_R$ a vector of size 5. In the GeoDIN experiments, where all the wells were top-to-bottom vertical wells, the corresponding well $CFs$ are set to $CF = 1$. The generalization of the GeoDIN model to incorporate, e.g., slanted wells, would encode $CF \neq 1$ values.

The $j$-$th$ columns of the $R_R$ and $R_S$ arrays represent one-hot encoding vectors that indicate the receiver and

sender object's indices, respectively.

The $m$ computes[21] the matrix products $O^T R_R$ $(\dim(O^T R_R)$ $= D_S \times N_R)$ and $O^T R_S$ $(\dim(O^T R_S) = D_S \times N_R)$ and concatenates them vertically with $R_I$:

$$m(G) = [O^T R_R; O^T R_S; R_I] = B \qquad 5$$

The resulting $B$ is a $(2D_S + D_R) \times N_R$ array, whose columns represent the interaction terms $b_k$ for the $N_R$ relations or edges in graph $G$. As indicated in Fig. 2, in GeoDIN implementation the $X$ are encoded as well object attributes into $m$.

$B$ represents an input to $\Phi_R$, which applies $f_R(\cdot)$, a NN, to each array column. In such manner, the $\Phi_R$ predicts

**Fig. 4** *The encoded relative permeability function used to augment the GeoDIN object's model.*
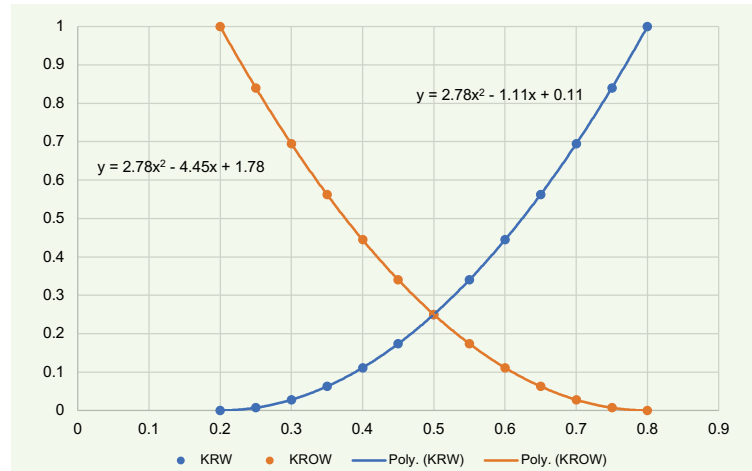
the effect of each interaction $e_k$ by applying $f_R(\cdot)$ to each $b_k$. The output of $f_R(\cdot)$ is a $D_E$ length effect vector, $e_k$, which represents an embedded distribution of calculated effects on objects ($O$). The role of $\Phi_R$ is to concatenate the $N_R$ effects to form the $D_E \times N_R$ effect array, $E$.

$G$ and $E$ are input to aggregation function $a$, which computes the $D_E \times N_O$ matrix product, $\bar{E} = ER_R^T$, whose $j$-th column equals to element-wise summation over all $e_k$ whose corresponding relation has a receiver object, $o_j$.

$$a(G, E) = [O^T; \bar{E}] = C \qquad 6$$

The resulting $C$ is a $(D_{SDyn} + D_E) \times N_O$ array whose $N_O$ columns are the object states and per object aggregated interaction effects.

To clarify, the GeoDIN model is applied to solve a forward problem, to predict the evolution of dynamic state variables, i.e., the future $t+1$ states of $SOIL$, and $SWAT$, and $PRESS$, while the state updates are not applied to $D_{SStat}$. Should the application of GeoDIN be reformulated to solve the inverse problem, e.g., static model reconciliation with dynamic data, referred to as history matching, then the array $C$ of the aggregated interaction effects would combine both, $D_{SDyn}$ and $D_{SStat}$.

$C$ is input to $\Phi_O$, which applies $f_O(\cdot)$, another NN, to each $N_O$ column. The output of $f_O(\cdot)$ is a $D_P$ length vector, $p_j$, and $\Phi_O$ concatenates them to form the output array $P$ ($\dim(P) = 3 \times N_O$) of which components are predicted vectors of $SOIL$, $SWAT$, and $PRESS$ per simulated time step.

We train the GeoDIN using multiple hidden layers with various numbers of neurons, gated by the ReLU activation function and optimized with a stochastic gradient-based optimizer (ADAM)[26]. The GeoDIN is comprised of two FFNNs: the first FFNN, the $\Phi_R$, calculates the $e_k$, and the second FFNN, the object model, learns to apply this $e_k$ on the $o_j$. During training, the objective is to minimize the loss of the object model, defined as a mean square error (MSE) between the model's prediction and the full physics simulation, per simulation time step, across all the objects:

$$loss = MSE\left(f_O(o_{j,t}, e_k), (o_{j,t+1})\right) \qquad 7$$

At this point it is worth clarifying that GeoDIN does not incorporate an explicit time integration as perceived for and implemented in the PINN frameworks[8]. In GeoDIN, the flow physics is captured from simulation models by learning object-to-object interaction terms and computing their effects to predict the next object states. As such, the GeoDIN loss function only incorporates data-driven terms. In PINNs, however, the flow physics is emulated, and loss function combines the terms for solving flow governing PDEs, the terms with associated initial and boundary conditions as well as data-driven terms. In Maucec and Jalali (2021)[27] we further demonstrate the assembly of the $O$ and $R$ arrays with implementation on a simplified example of $3 \times 3 \times 1$ simulation grid with a corner injector and producer.

**Experiments:** We use the data for 800 days out of 1,827 days of simulated production for training. The FFNN was trained for 500 epochs. Figure 5 shows the convergence

of model loss function and the convergence of the mean cell error as a contribution from the individual predicted response terms, $SOIL$, $SWAT$, and $PRESS$.

In Table 2 we list the GeoDIN model training time, for models presented in Fig. 6. The timing values correspond

**Fig. 5**  *The training error convergence of the GeoDIN model: (a) the model loss as MSE between the model's prediction and the full physics simulation, and (b) contribution of individual predicted response terms, SOIL, SWAT, and PRESS, to the cell mean error.*
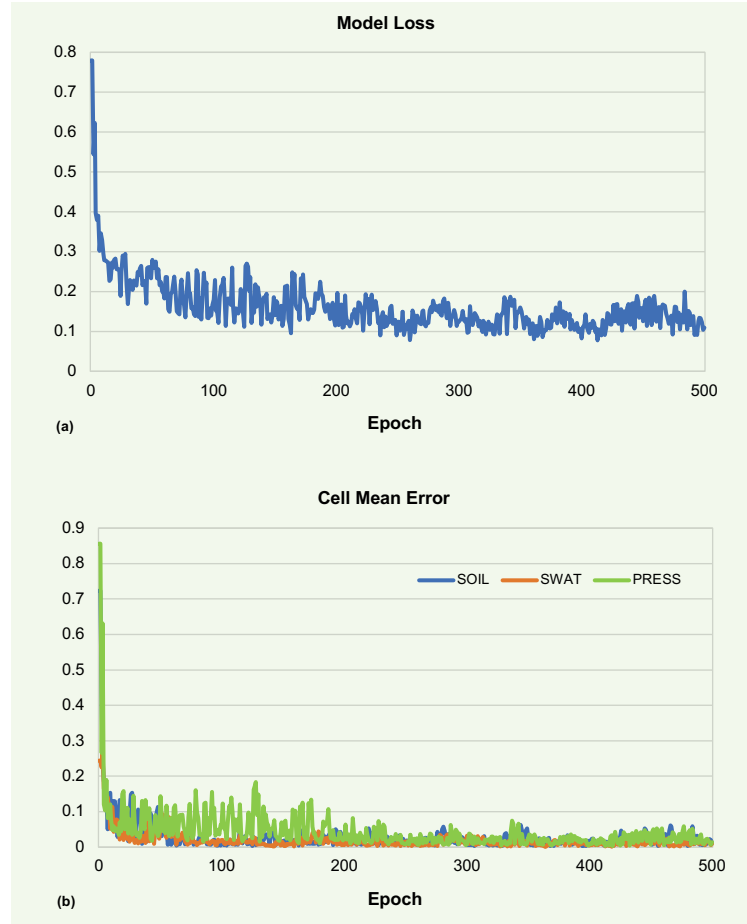


**Table 2**  *The GeoDIN model training time for models presented in Fig. 6.*

| No. of Layers | Training (min) |
|---|---|
| 3 | 4.4 |
| 5 | 3.3 |
| 10 | 7.7 |
| 20 | 15.4 |
| 40 | 30.3 |
| 80 | N/A |

to the use of a single GPU for all the models. The 80-layer model was not used for training to avoid memory allocation problems. Note that the training time values, as listed do not correspond to run time. They are only reported for evaluation purposes, but not used for prediction.

The prediction performance of the GeoDIN model was benchmarked against the full physics simulation run. The full physics simulation runs were performed on 70 Intel Xeon E5 CPU cores. The prediction period was 1,827 days. In Fig. 6, we show the run time performance as a function of the model size, by increasing the number of vertical layers from 3, 5, 10, 20, and 40, to 80. For the model sizes with a number of layers up to 40, a single V100 GPU was used to run the GeoDIN model predictions, for the model with 80 vertical layers, two GPUs were used to meet the memory requirements. Herewith, the run time corresponds to the rollout of 1,827 daily time steps in prediction mode.

While the predictive run time performance of full physics and GeoDIN model is comparable for the smallest model size (after discounting for the difference in hardware), the later model demonstrates significantly faster prediction for larger size models. In particular, when using the two GPUs vs. 70 CPUs, the GeoDIN prediction is almost five times faster.

In Fig. 7 we compare the number of relations (graph edges in the GeoDIN model) and the size of underlying simulation grid model as a function of the number of K-layers in the represented SPE10 model. The annotated trendlines indicate a linear dependence on the number of K-layers for both, the simulation grid size and the number of graph relationships. Consequently, the size of the graph increases approximately six times faster than the size of the grid. In practical terms, this suggests that with model scale up, the expansion of the network graph, as a representation of the reservoir simulation grid, potentially poses a challenge for interaction network training, due to the GPU memory limitations.

We have performed three prediction experiments with GeoDIN while benchmarking against a full physics reservoir simulator. It is important to note that the same full physics simulation model with three top layers from the upper shallow marine formation, was used to train all three GeoDIN predictive models.

1. **Experiment 1:** Perform prediction of spatiotemporal dynamics of *SOIL*, *SWAT*, and *PRESS* in the same three model layers as used for training. *SOIL* and *SWAT* were predicted independently and not constrained by the mass conservation equation for two-phase flow, i.e., $SOIL + SWAT = 1$. We have considered such an approach to investigate the predictive capability of the GeoDIN framework when generalized to three-phase gas/oil/water systems. The derivation of a gaseous component from three-phase mass conservation equation as $SGAS = 1 - SOIL - SWAT$, requires the independent prediction of oil and water components.

2. **Experiment 2:** Do not retrain the GeoDIN model, relocate the water injector to a different position in the



*Fig. 6   The run time performance of the GeoDIN model (orange) against the full physics simulation model (blue) as a function of the model size for the rollout of 1,827 daily time steps in prediction mode.*
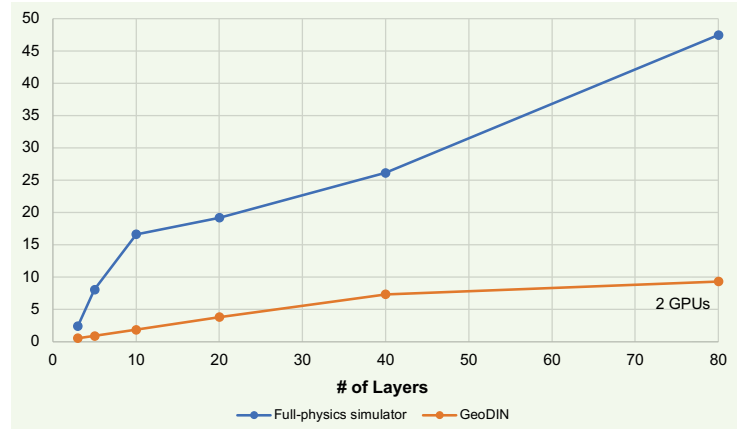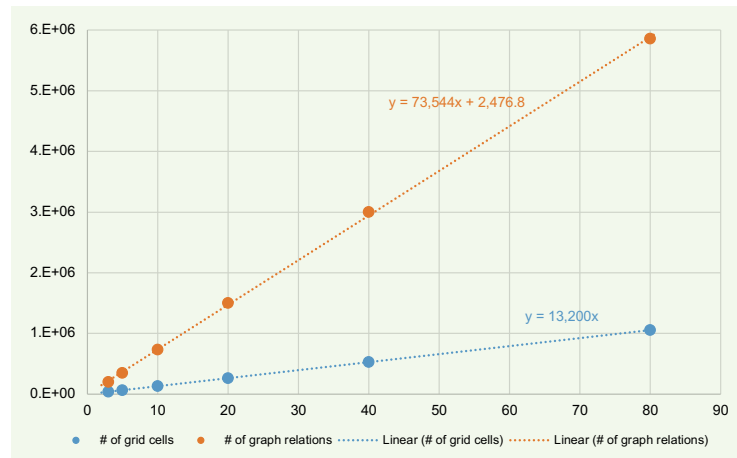


*Fig. 7   The number of relations (graph edges in GeoDIN model; orange) and grid cells in the underlying full physics simulation model (blue) vs. number of K-layers.*

simulation grid (Fig. 8; top row) and perform prediction of spatiotemporal dynamics of *SOIL*, *SWAT*, and *PRESS* in the same three-layer model. The objective of this experiment was to investigate how accurately the GeoDIN model can capture spatiotemporal flow dynamics with perturbed injector location, mimicking a stage of simplified infill drilling plan.

3. **Experiment 3:** As previously outlined, the SPE10 reservoir model under study consists of two distinctive formations, where in the top 35 shallow marine layers the permeability is relatively smooth, while in the bottom 50 layers follows a fluvial channel spatial distribution (Fig. 8; bottom row). Both formations are characterized by large permeability variations between eight to 12 orders or magnitude. The objectives of this experiment were to:

• Learn the representative fluid flow dynamics in

**Fig. 8** *The visualization of information complimentary to a specific GeoDIN prediction experiment: relocation of the water injector in the simulation grid in Experiment 2 (top) and visualization of X-permeability in distinctive formations, corresponding to top shallow marine formation and bottom fluvial channel formation in Experiment 3 (bottom). In the top panel, the appearance of dark-colored clusters of points, corresponding to inactive cells is marked for clarification.*
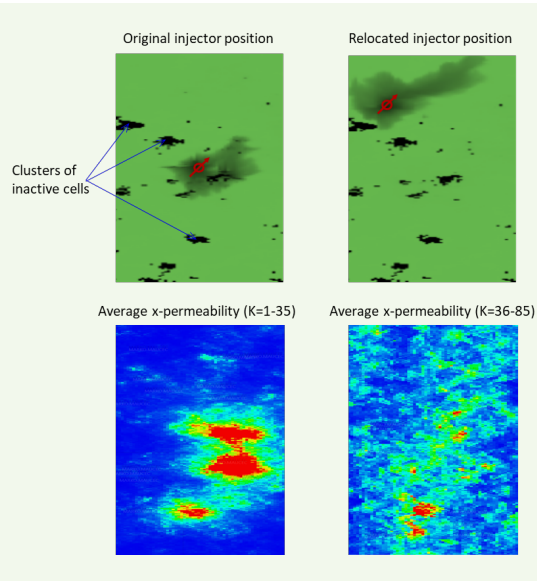
shallow marine subsurface depositions and predict the spatiotemporal flow dynamics in the 85-layer model.

- Compare GeoDIN predicted spatiotemporal flow dynamics in a layer, selected from the bottom formation with the full physics simulation model.

The SPE10 simulation grid contains approximately 2.5% of inactive cells. In the simulation model, the inactive cells are assigned zero porosity and are not considered in flow calculations with full physics PDE solvers. In GeoDIN, we remove inactive cells from the graph, i.e., we ignore inactive cells when we convert the simulation model grid to a graph. Subsequently, we maintain one-on-one correspondence or mapping between the simulation grid and the generated graph by preserving the exact spatial location of inactive cells when the graph is converted back to the grid. In visualization of pressure and saturation maps, the inactive cells appear as dark-color clusters or ghost regions of points, Fig. 8. The same correspondence applies to pressure and saturation maps, previously noted.

## Results

### Experiment 1: Prediction of Fluid Flow Dynamics in Three-Layer Model

Figures 9 to 11 provide a comparison between the GeoDIN prediction and full physics simulation for the *SOIL*, *SWAT*, and *PRESS*, respectively. We visualize the property maps for a selected layer (K = 2) of the

three-layer simulation model. The represented fluid flow dynamics corresponds to a centrally located injector.

The presentation format is as follows:

- The top panel shows the snapshots of dynamic flow property predicted with the GeoDIN model at four time steps: 3 days, 500 days, 1,000 days, and 1,600 days.
- The central panel shows the snapshots of dynamic flow property predicted with a full physics simulator at the same time steps.
- The bottom panel shows the spatial map of a logarithm (for visualization purposes) square error per cell between the GeoDIN predicted and full physics simulated dynamic flow property at the same time steps.
- The unified color scales used are green for oil, blue for water, magenta for pressure, and red for square error.

Figure 12 outlines the boxplots of per cell error distribution for the GeoDIN prediction relative to full physics simulation for *SOIL*, *SWAT*, and *PRESS*, respectively, as a function of the simulation/prediction time step. The statistical error analysis corresponding to the final time step — end of simulation/prediction — indicates that the mean absolute error in *SOIL* is approximately 2%. The error distribution suggests that 50% of grid cells fall within a 4% error bound, while 90% of the grid cells fall within a 5% error bound. For *SWAT*, the mean absolute error is approximately 0.5%. The error distribution suggests that 50% of the grid cells fall within a 1.5% error bound, while 90% of the grid cells fall within a 2.5% error bound. For the *PRESS*, while the mean absolute error is approximately 5%, the error distribution suggests that 90% of grid cells fall within a 20% error bound, indicating that the GeoDIN model prediction overestimates the simulated pressure.

The spatiotemporal propagation of pressure is more sensitive to local embeddings of interaction networks, which communicate on node-to-node information transfer. The representation of reservoir pressure dynamics in the SPE10 model is governed by initial pore fluid distribution. This characterizes pressure as a global physics property, establishing several orders of magnitude faster than the fluid convection speed[11]. The external pressure support comes in the form of a single water injector, and in training, the GeoDIN framework fails to capture meaningful small variability in induced pressure dynamics, which results in a larger prediction error when benchmarked with full physics simulation.

### Experiment 2: Prediction of Fluid Flow Dynamics in Three-Layer Model with Relocated Water Injector

Figures 13 to 15 provide a comparison between the GeoDIN prediction conducted in Experiment 2, and full physics simulation for *SOIL*, *SWAT*, and *PRESS*, respectively. We visualize the property maps for a selected layer (K = 2) of the three-layer simulation model. The represented fluid flow dynamics corresponds to a relocated water injector, as previously discussed.

Figure 16 outlines the boxplots of per cell error distribution for the GeoDIN prediction relative to full physics

**Fig. 9**  *A comparison of* SOIL *maps between the GeoDIN prediction and full physics simulation for a selected layer (K = 2) of the three-layer simulation model (Experiment 1) over time. The dark-colored clusters of points correspond to inactive cells.*
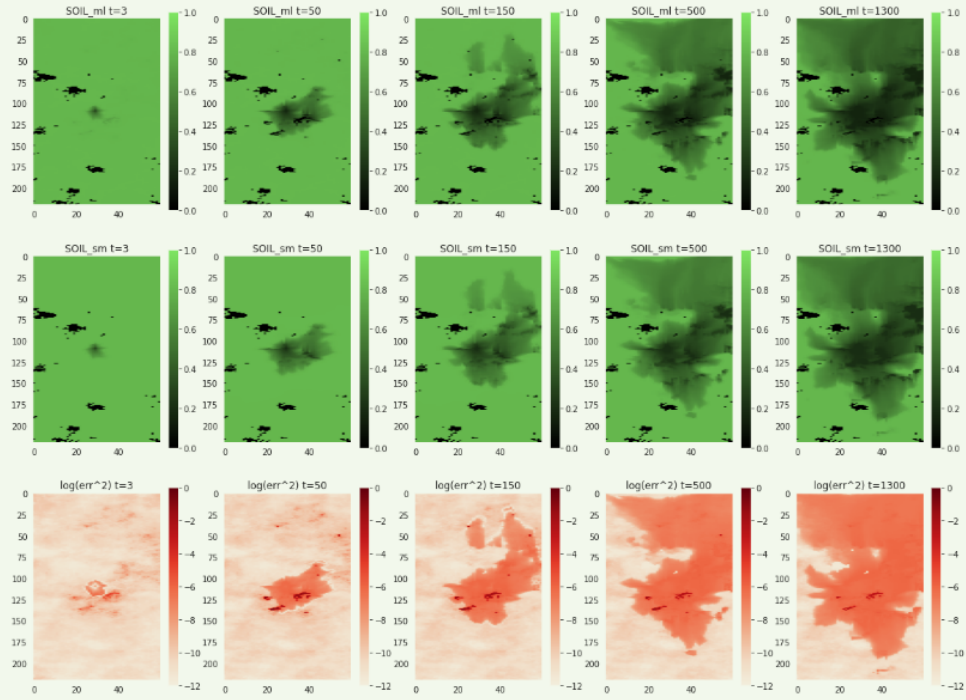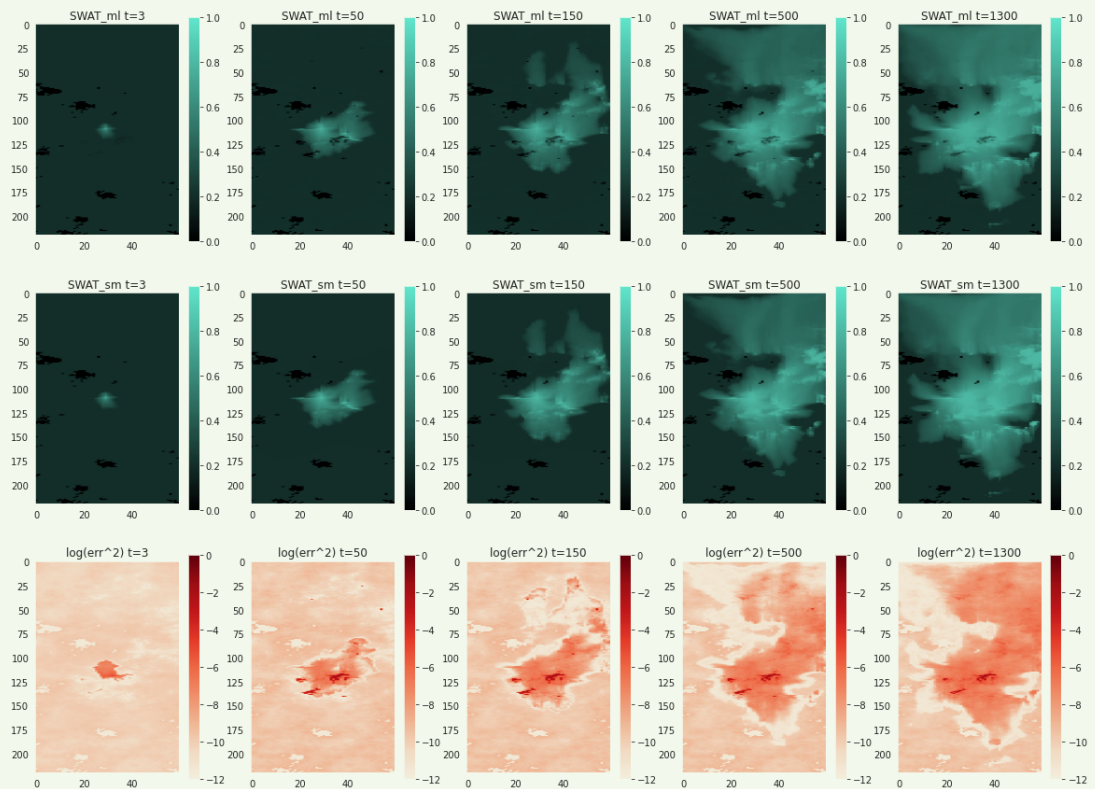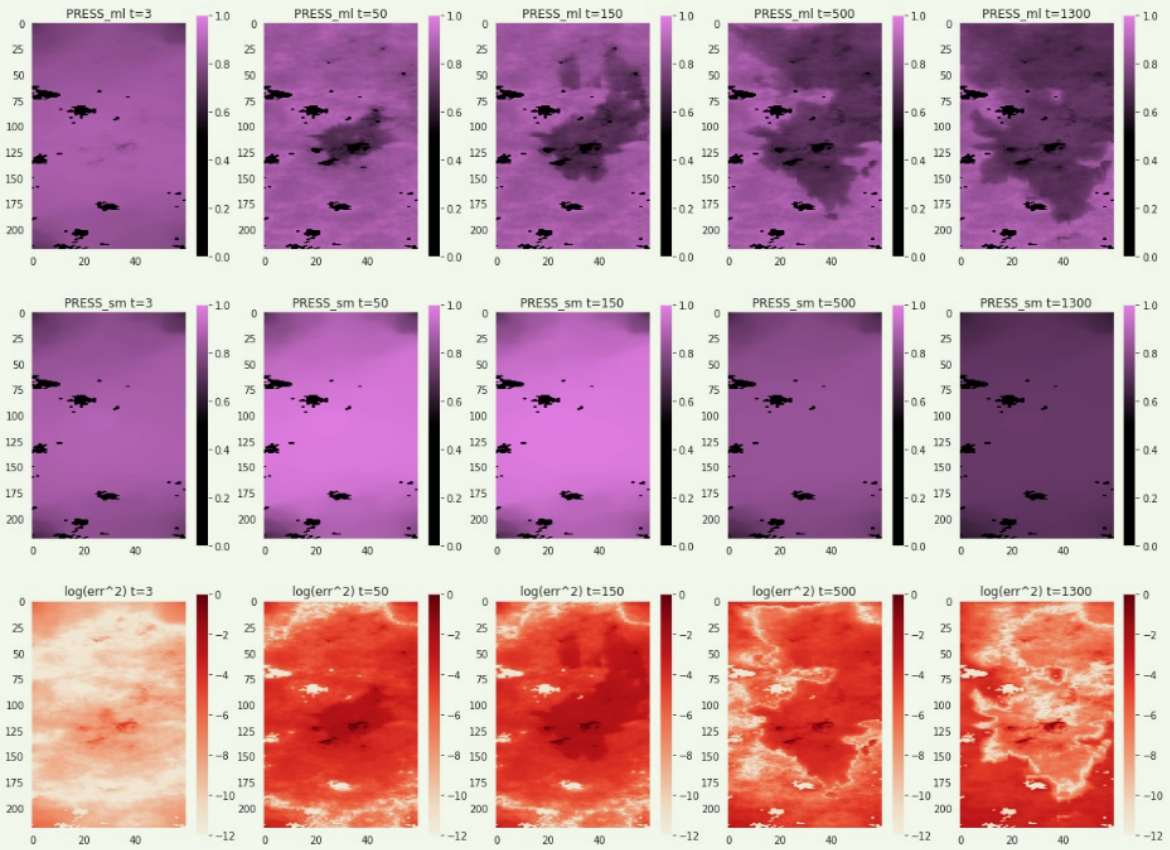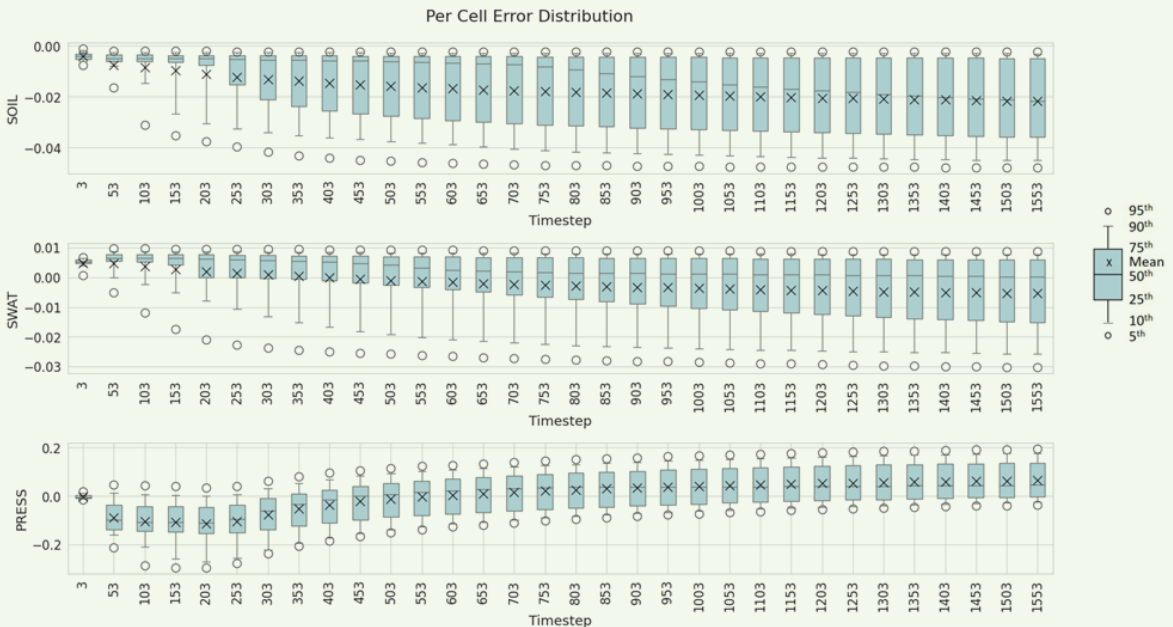


**Fig. 10**  *A comparison of* SWAT *maps between the GeoDIN prediction and full physics simulation for a selected layer (K = 2) of the three-layer simulation model (Experiment 1) over time. The dark-colored clusters of points correspond to inactive cells.*

**Fig. 11**  *A comparison of normalized PRESS maps between the GeoDIN prediction and full physics simulation for a selected layer (K = 2) of the three-layer simulation model (Experiment 1) over time. The dark-colored clusters of points correspond to inactive cells.*



**Fig. 12**  *The per cell error distribution for the GeoDIN prediction relative to full physics simulation for SOIL, SWAT, and PRESS, respectively, in a three-layer simulation model (Experiment 1), over time.*

**Fig. 13**  *A comparison of SOIL maps between the GeoDIN prediction and full physics simulation for a selected layer (K = 2) of the three-layer simulation model with relocated injector (Experiment 2), over time. The dark-colored clusters of points correspond to inactive cells.*
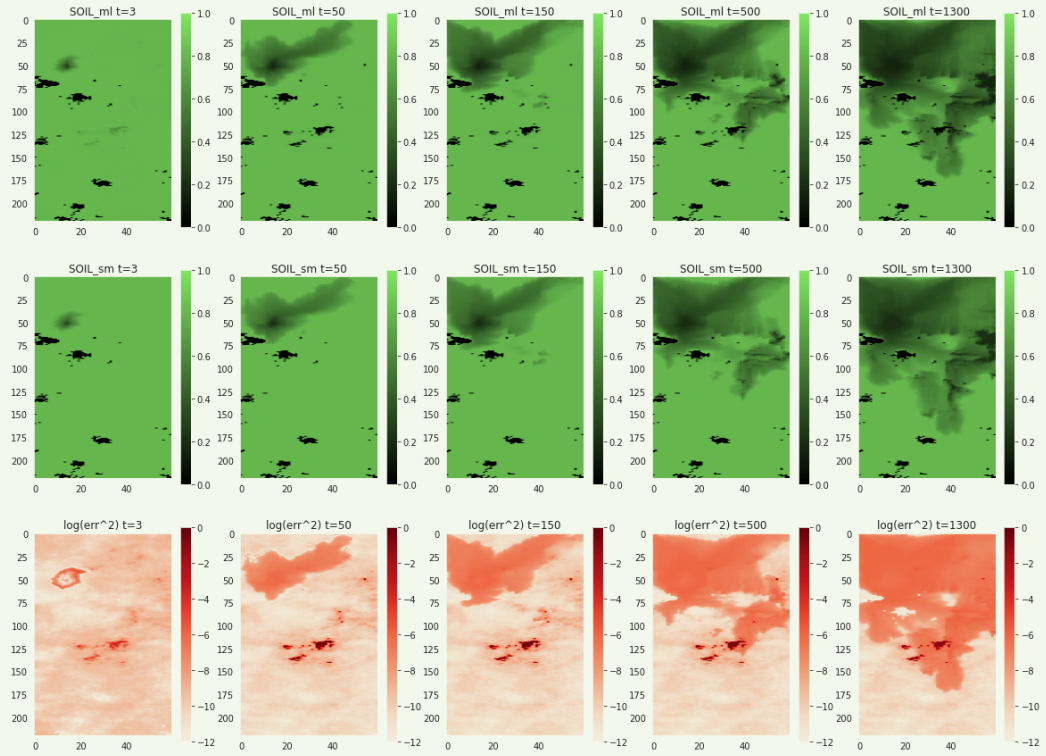


**Fig. 14**  *A comparison of* SWAT *maps between the GeoDIN prediction and full physics simulation for a selected layer (K = 2) of the three-layer simulation model with relocated injector (Experiment 2), over time. The dark-colored clusters of points correspond to inactive cells.*
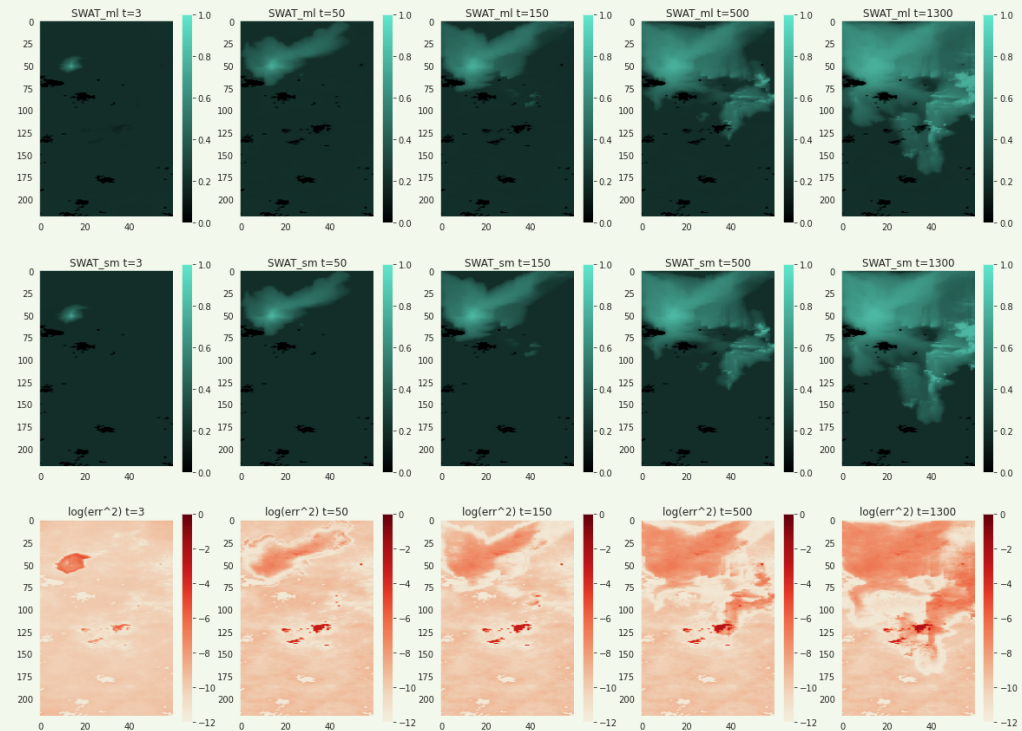
**Fig. 15**  *A comparison of PRESS maps between the GeoDIN prediction and full physics simulation for a selected layer (K = 2) of the three-layer simulation model with relocated injector (Experiment 2), over time. The dark-colored clusters of points correspond to inactive cells.*
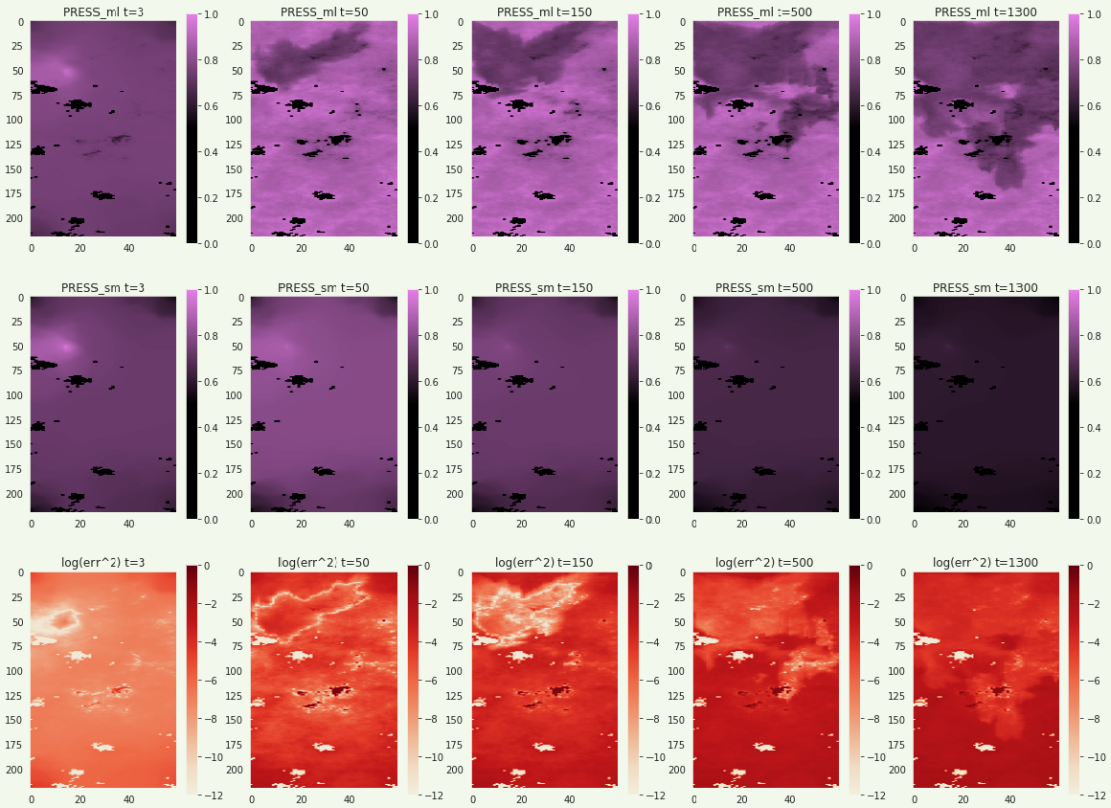


**Fig. 16**  *The per cell error distribution for the GeoDIN prediction relative to full physics simulation for SOIL, SWAT, and PRESS, respectively, in a three-layer simulation model with relocated injector (Experiment 2), over time.*
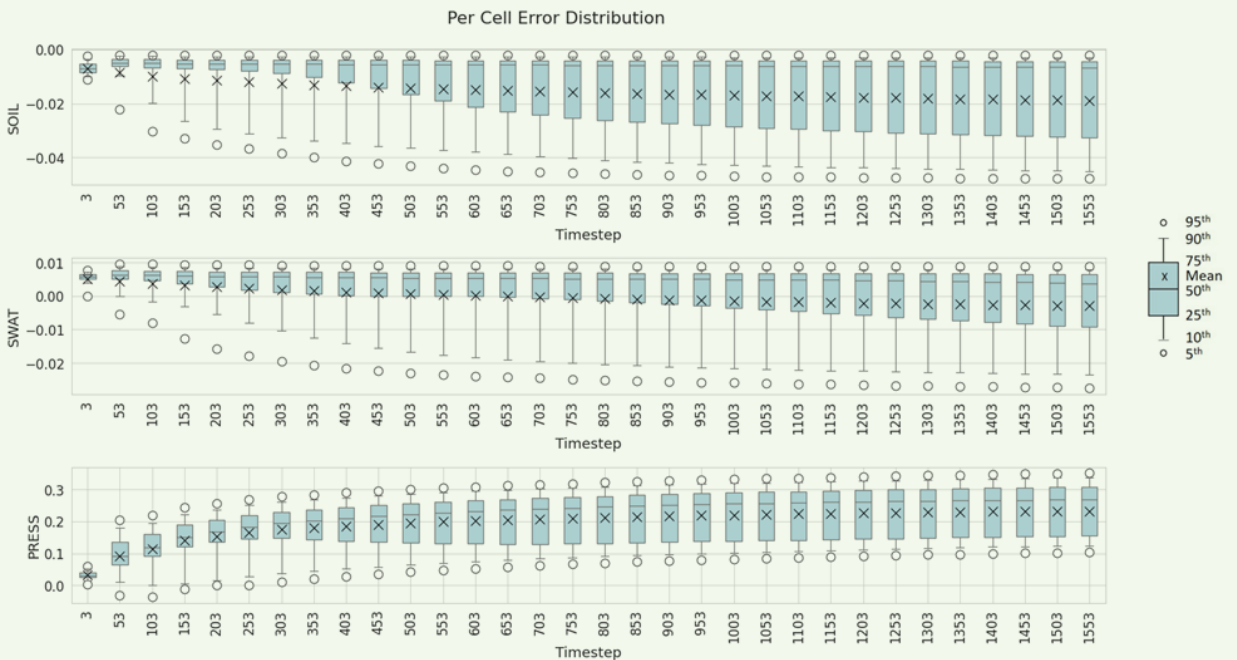
**Fig. 17** *A comparison of* SOIL *maps between the GeoDIN prediction and full physics simulation for a selected layer (K = 55) of the 85-layer simulation model (Experiment 3), over time. The dark-colored clusters of points correspond to inactive cells.*



**Fig. 18** *A comparison of* SWAT *maps between the GeoDIN prediction and full physics simulation for a selected layer (K = 55) of the 85-layer simulation model (Experiment 3), over time. The dark-colored clusters of points correspond to inactive cells.*

**Fig. 19**  *A comparison of* PRESS *maps between the GeoDIN prediction and full physics simulation for a selected layer (K = 55) of the 85-layer simulation model (Experiment 3), over time. The dark-colored clusters of points correspond to inactive cells.*
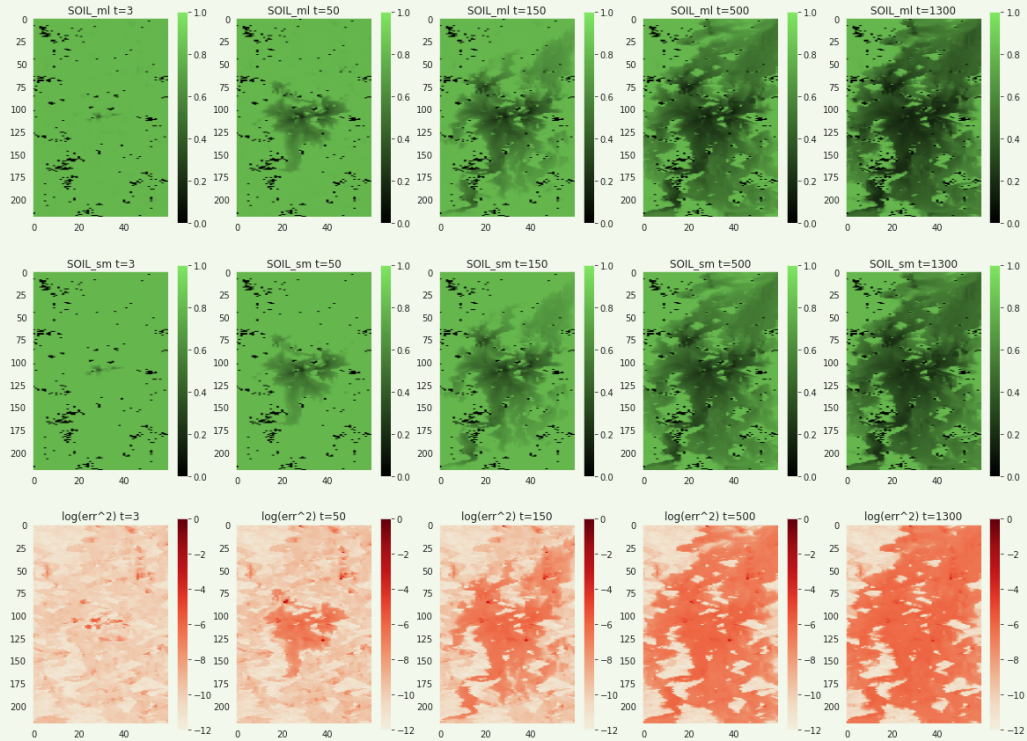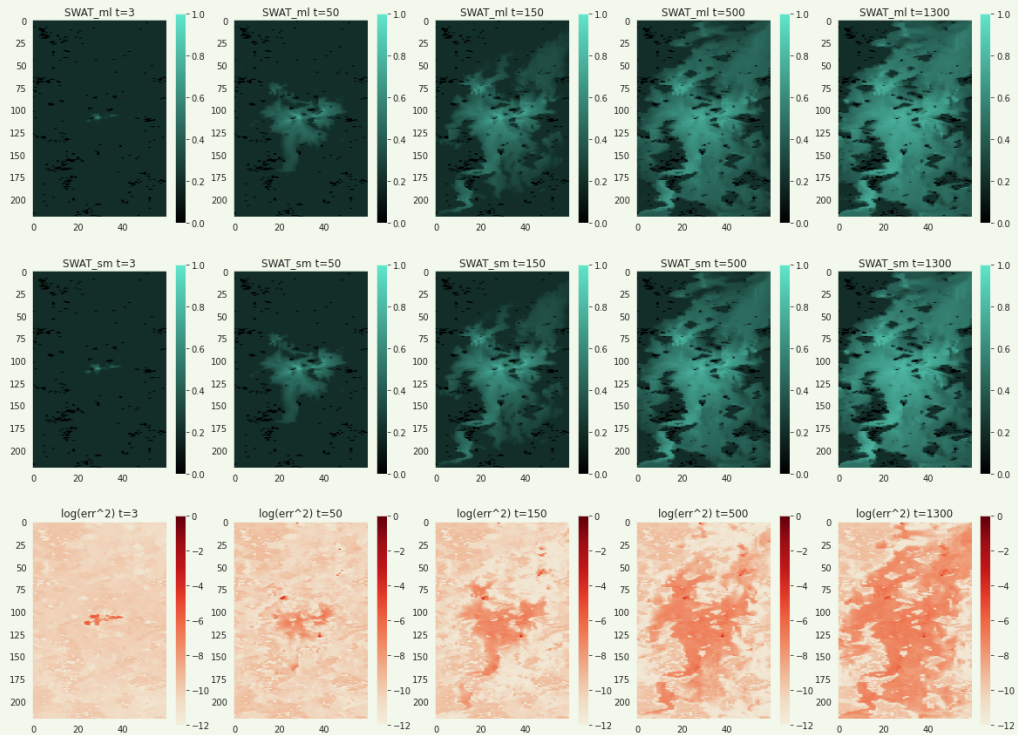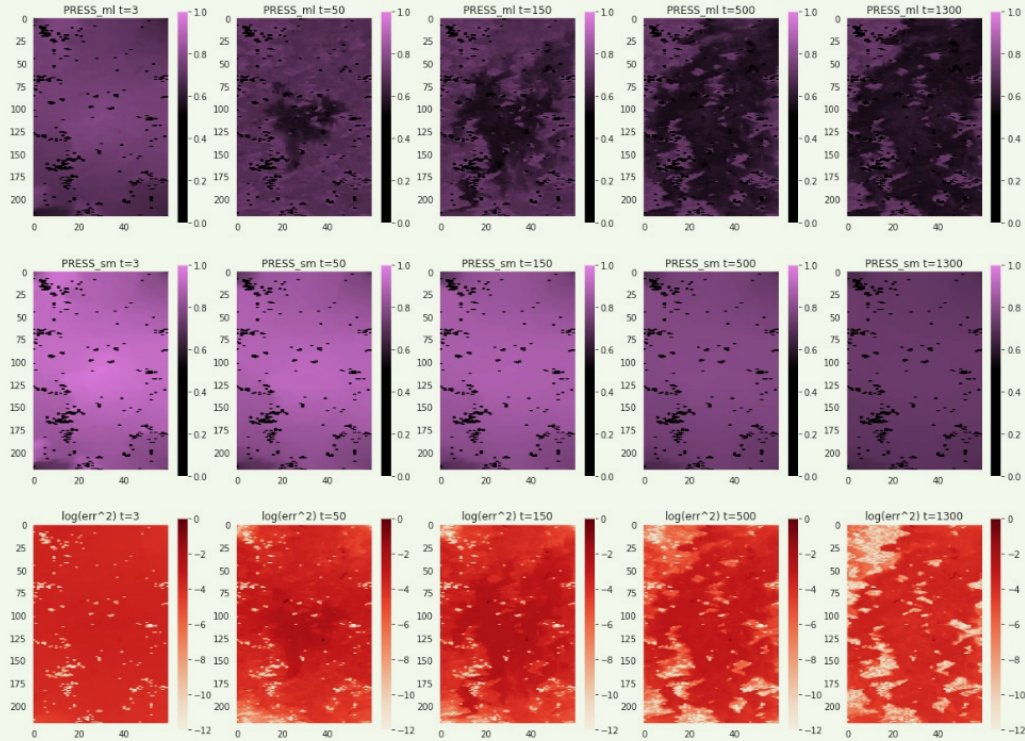


simulation for *SOIL*, *SWAT*, and *PRESS*, respectively, as a function of simulation/prediction time step. The statistical error analysis corresponding to the final time step — end of simulation/prediction — indicates the mean absolute error in *SOIL* is approximately 2%. The error distribution suggests that 50% of the grid cells fall within a 3% error bound, while 90% of the grid cells fall within a 4.5% error bound. For *SWAT*, the mean absolute error is approximately 0.5%. The error distribution suggests that 50% of the grid cells fall within a 1% error bound, while 90% of the grid cells fall within a 2.5% error bound. For *PRESS*, the mean absolute error is approximately 23%, while the error distribution suggests that 90% of the grid cells fall within a 10% to 30% error bound, indicating that the GeoDIN model prediction overestimates the simulated reservoir pressure. The physical reasoning behind the phenomenon refers to the explanation previously discussed.

**Experiment 3: Prediction of Fluid Flow Dynamics in Distinctively Different Formation of 85-Layer Model**

In experiment 3, the GeoDIN model was trained with the three-layer full physics simulation model of the upper formation and learned the representative fluid flow dynamics in the upper shallow marine subsurface depositions. The model was then used to predict the spatiotemporal flow dynamics in the 85-layer model. We visualize the fluid distribution maps in a selected layer (K = 55) corresponding to the lower fluvial channel

formation of the 85-layer simulation model. Figures 17 to 19, respectively, correspond to *SOIL*, *SWAT*, and *PRESS*.

The results demonstrate the ability of the GeoDIN model to learn the fluid dynamics from the three-layer model and accurately generalize the interaction effects on a larger — 85-layer — simulation grid model with distinctively different distribution of matrix permeability, spatially, and by magnitude. We augment the outcome by interpreting Fig. 20, which shows the results of *TRANS* normalization for data points corresponding to active cells, using Box-Cox transformation. The upper row corresponds to the transmissibility from three-layer simulation model used for GeoDIN training, while the bottom row corresponds to transmissibility of the 85-layer model used for prediction.

The *TRANS*, extracted from the full physics simulation output, is severely right-skewed and resembles power law distribution with extreme values reaching up to 600,000. The transformation of the *TRANS* into a distribution that resembles normality is essential because in general, for the NNs, the learning from highly imbalanced data with power-law-like distributions can be quite challenging. Moreover, since transmissibility represents the main relation/edge attribute in the network graph model that controls cell-to-cell communication via diffusivity, the outlier removal is not recommended.

It is interesting to observe that the Box-Cox transformation of model transmissibility renders a multimodal

distribution for the 85-layer model, which clearly indicates the presence of distinctive formations as well as flow units in a subsurface model. Moreover, as shown by the boxplots in the right column of Fig. 20, the shapes of transformed density distributions of three-layer and 85-layer models are statistically sufficiently similar for GeoDIN to learn spatial fluid dynamics in the three-layer model and accurately predict in the 85-layer model.

Figure 21 outlines the boxplots of per cell error distribution for the GeoDIN prediction relative to full physics simulation for the *SOIL*, *SWAT*, and *PRESS*, respectively, as a function of simulation/prediction time step. The statistical error analysis corresponding to the final time step — end of simulation/prediction — indicates the mean absolute error in *SOIL* is approximately 2%. The error distribution suggests that 50% of the grid cells fall within a 3.8% error bound, while 90% of the grid cells fall within a 4.5% error bound. For the *SWAT*, the mean absolute error is approximately 0.5%. The error distribution suggests that 50% of the grid cells fall within a 1.5% error bound, while 90% of the grid cells fall within a 2.5% error bound. For *PRESS*, the mean absolute error is approximately 8%, while the error distribution suggests that 95% of the grid cells fall within a 20% error bound, indicating that the GeoDIN model prediction underestimates the simulated reservoir pressure. The physical reasoning behind the phenomenon refers to the explanation previously discussed.

## Discussion

We introduced the GeoDIN framework that learns complex representations of subsurface from reservoir simulation models and predicts 3D flow dynamics. We conducted various experiments and demonstrated that, on average, the error in GeoDIN predicted spatiotemporal distribution of *SOIL* remains within 5% of full physics simulation for 90% of the model grid cells, while the error in *SWAT* remains within 2.5% of the full physics simulation.

Subsequently, with its current architecture, the GeoDIN cannot accurately predict the well production rates for oil and water. The GeoDIN is based on the concept of interaction networks[21], initially developed and validated for tasks of physical reasoning such as predicting potential energy of $n$-body systems, where $n$ interacting objects are of the same type and result in $n(n-1)$ relations to learn meaningful interactions caused by exerting distance and mass dependent forces on each other.

As previously described, the GeoDIN graph representation of the reservoir simulation model embodies two types of objects (nodes): grid cells and wells. The dominant interaction dynamics occurs at cell-to-cell level and the three-layer model, used in our training experiments, renders almost 200,000 relations (graph edges in the GeoDIN model) to accurately learn meaningful cell-to-cell flow dynamics by interaction networks.

In GeoDIN, *CFs* are used to one-hot encode wells

**Fig. 20** *Results of transmissibility normalization for data points corresponding to active cells, using Box-Cox transformation.*
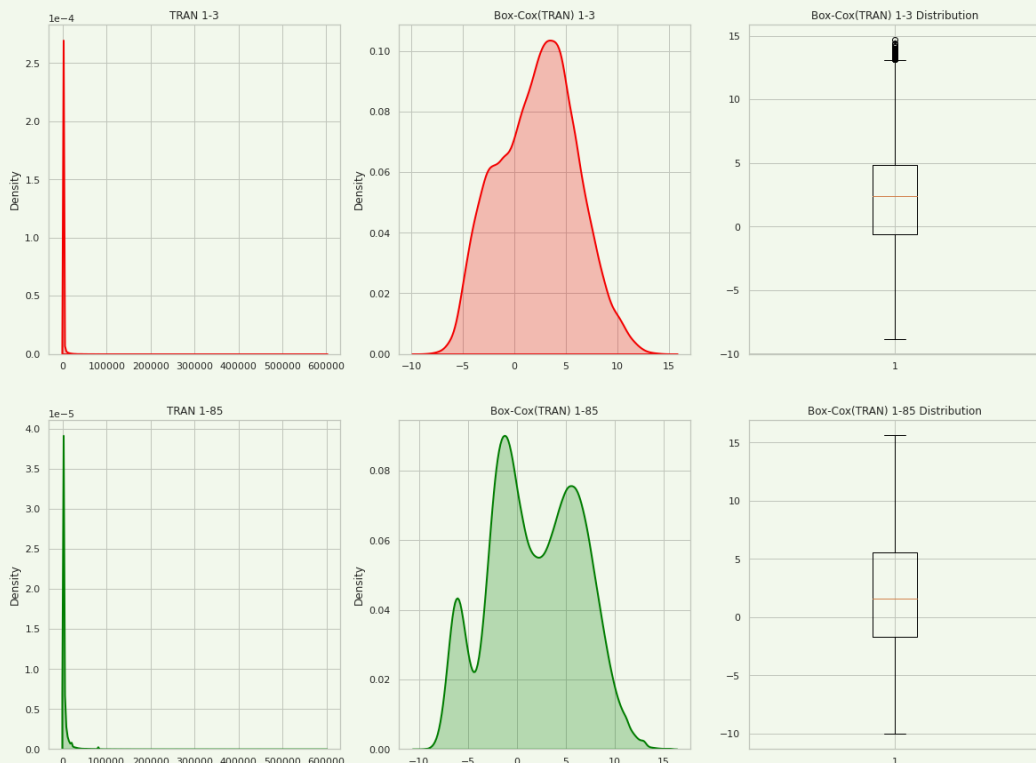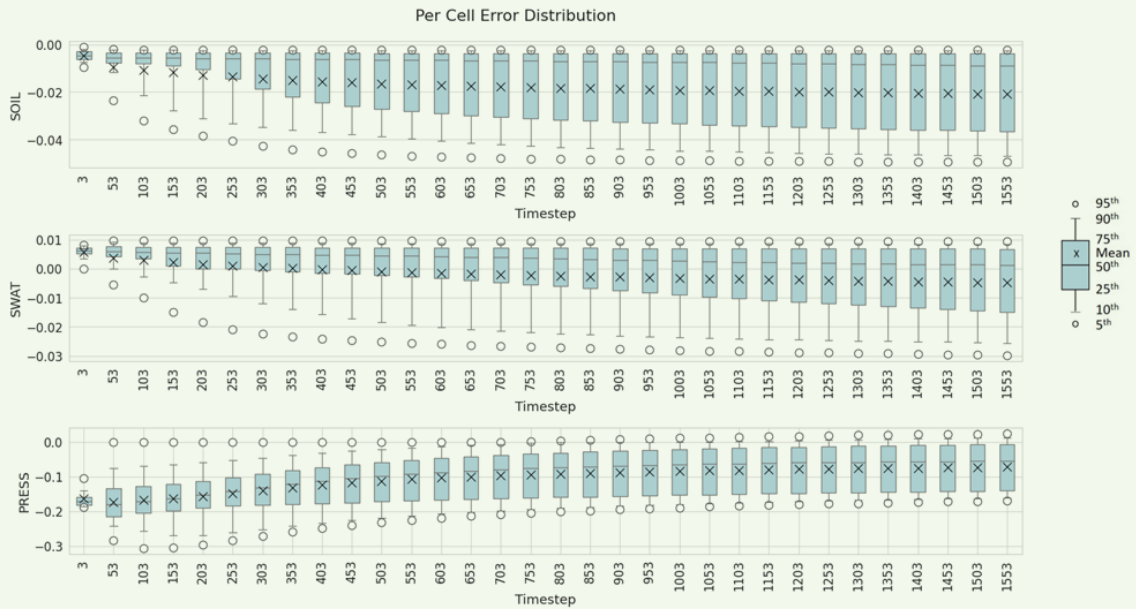
**Fig. 21** *The per cell error distribution for the GeoDIN prediction relative to full physics simulation for SOIL, SWAT, and PRESS, respectively, in the 85-layer simulation model (Experiment 3), over time.*



into a network graph. In the three-layer model, used for training, encoding five wells (one injector and four producers), completed top-to-bottom results in 15 well-to-cell relations. This is orders of magnitude lower than the number of cell-to-cell relations and insufficient for interaction networks to learn meaningful well-to-cell dynamics and accurately predict well rates. Alternative approaches can be investigated to improve the prediction of well rates in GeoDIN models: (a) predict flow saturation within drainage regions of perforated/completed well cells with interaction networks (expansion to drainage regions will increase the number of corresponding well-to-cell relations) and use separate machine learning models such as multilayer perception, LSTM, or recurrent NN to predict well rates as time series, and (b) modify the loss function to penalize for the well-to-cell interactions in prediction of well rates.

## Conclusions

GeoDIN is a novel proof-of-concept technology with applications to graph learning from reservoir simulation models that carries a game changing potential for rapid prediction of subsurface flow dynamics. For *SOIL* and *SWAT*, the GeoDIN model prediction generalizes efficiently to capture the interaction effects on a larger simulation grid model with distinctively different distribution of subsurface properties, spatially, and by magnitude (Experiment 3). Furthermore, a high degree of generalization has been achieved to account for variable (injector) well locations (Experiment 2). In addition, we demonstrate a significant prediction speed up of the GeoDIN model with respect to full physics simulation reaching almost fivefold acceleration for the largest model simulated, with reduced hardware requirements (two

GPUs vs. 70 CPUs).

When training the GeoDIN model, the GPU memory allocation may become challenging with model scale up. In our experiments with the SPE10 model, the number of graph edges increases almost six times faster than the number of cells in the underlying simulation grid. The graph size may expand at even higher rates when distinctive features that govern reservoir connectivity, e.g., fractures, faults, and high flow units, are encoded. One recommendation would be to utilize the distributed deep learning training framework (Horovod) and leverage state-of-the-art hardware, such as GPU clusters with sufficient memory to perform the training at scale. It is also suggested to build on the learnings from Box-Cox data transformation and perform a rigorous sensitivity and ranking analysis, jointly for network graph object and relation attributes, and with variable well positioning to evaluate their distinctive impact on learning cell-to-cell flow diffusivity.

When compared to fluid dynamics, the reservoir pressure is characterized as the global model property, established several orders of magnitude faster than the fluid convection speed. In interaction networks, which communicate by node-to-node information transfer, the spatiotemporal propagation of pressure is more sensitive to local embeddings, which makes the learning of representative pressure dynamics significantly more challenging. The GeoDIN model is unable to accurately capture meaningful pressure dynamics induced by a single water injector, which results in a larger prediction error when benchmarked with reservoir simulation.

On average, over the three conducted experiments, the error distribution suggests that a great majority (90% to

95%) of grid cells fall within 10% to 30% error bound relative to full physics simulation. The ability of GeoDIN to predict spatial pressure dynamics more accurately could improve if the model is trained with a variable number and use locations of injectors as well as variable injection rates. We may conduct such experiments in the future.

As the way forward, we are currently investigating the application of the state-of-the-art NN architectures, such as graph NNs with advanced feature encoding and augmentation to improve training with clustered and sectorized data, learn highly similar graph structures and embeddings, propagate information across graphs with automated feature learning, and to conserve fluid volumes over long prediction times. Ultimately, our objective is to generalize and scale up the GeoDIN architectures by training with reservoir properties under uncertainty, a variety of scenarios of distinctive reservoir connectivity (faulted and fractured models), complex structure and gridding, e.g., unstructured and locally refined grids, and with modeling different recovery drive mechanisms, improved oil recovery strategies, and well placement and production constraints.

## Acknowledgments

## References

1. Willcox, K.E., Ghattas, O. and Heimbach, P.: "The Imperative of Physics-Based Modeling and Inverse Theory in Computational Science," *Nature Computational Science*, Vol. 1, March 2021, pp. 166-168.

2. Zhao, Y. and Sarma, P.: "A Benchmarking Study of a Novel Data Physics Technology for Steamflood and SAGD Modeling: Comparison to Conventional Reservoir Simulation," SPE paper 189772, presented at the SPE Canada Heavy Oil Technical Conference, Calgary, Alberta, Canada, March 13-14, 2018.

3. Klie, H., Yan, B. and Klie, A.: "Transfer Learning for Scalable Optimization of Unconventional Field Operations," paper presented at the SPE/AAPG/SEG Unconventional Resources Technology Conference, Virtual, July 20-22, 2020.

4. Zhang, J., Cheung, S.W., Efendiev, Y., Gildin, E., et al.: "Deep Model Reduction Model Learning for Reservoir Simulation," SPE paper 193912, presented at the SPE Reservoir Simulation Conference, Galveston, Texas, April 10-11, 2019.

5. Jin, Z.L., Liu, Y. and Durlofsky, L.J.: "Deep Learning-Based Reduced Order Modeling for Subsurface Flow Simulation," 2019, *arXiv:1906.03729v1*.

6. Al-Sulaimani, T. and Wheeler, M.: "Reduced Order Modeling for Multiphase Flow Using a Physics-Based Deep Learning," SPE paper 203965, presented at the SPE Reservoir Simulation Conference, Galveston, Texas, October 4-6, 2021.

7. Watter, M., Springenberg, J.T., Boedecker, J. and Riedmiller, M.: "Embed to Control: A Locally Linear Latent Dynamics Model for Control from Raw Images," paper presented at the 29th Conference on Neural Information Processing Systems, Montreal, Quebec, Canada, December 7-12, 2015.

8. Fraces, C.G., Papaioannou, A. and Tchelepi, H.: "Physics Informed Deep Learning for Transport in Porous Media. Buckley Leverett Problem," 2020, *arXiv:2001.05172v1*.

9. Wang, N., Zhang, D., Chang, H. and Li, H.: "Deep Learning of Subsurface Flow via Theory-Guided Neural Network," *Journal of Hydrology*, Vol. 584, May 2020.

10. Wang, N., Chang, H. and Zhang, D.: "Efficient Uncertainty Quantification and Data Assimilation via Theory-Guided Convolutional Neural Network," *SPE Journal*, Vol. 26, Issue 6, December 2021, pp. 4128-4156.

11. Thavarajah, R., Zhai, X., Ma, Z. and Castineira, D.: "Fast Modeling and Understanding Fluid Dynamics Systems with Encoder-Decoder Networks," 2020, *arXiv:2006.05409v1*.

12. Cai, S., Mao, Z., Wang, Z., Yin, M., et al.: "Physics-Informed Neural Networks (PINNs) for Fluid Mechanics: A Review," 2021, *arXiv:2105.09506v1*.

13. Fuks, O. and Tchelepi, H.A.: "Limitations of Physics Informed Machine Learning for Nonlinear Two-Phase Transport in Porous Media," *Journal of Machine Learning for Modeling and Computing*, Vol. 1, Issue 1, 2020, pp. 19-37.

14. Zitnik, M., Agrawal, M. and Leskovec, J.: "Modeling Polypharmacy Side Effects with Graph Convolutional Networks," *Bioinformatics*, Vol. 34, Issue 13, July 2018, pp. i457-i466.

15. Hamilton, W.L., Ying, R. and Leskovec, J.: "Representation Learning on Graphs: Methods and Applications," *IEEE Data Engineering Bulletin*, Vol. 40, Issue 3, 2017, pp. 52-74.

16. Halac, D., Bhooshan, S., Chen, M., Abida, K., et al.: "Drive2Vec: Multiscale State-Space Embedding of Vehicular Sensor Data," paper presented at the IEEE International Conference on Intelligent Transportation Systems, Maui, Hawaii, November 4-7, 2018.

17. Cranmer, M.D., Xu, R., Battaglia, P. and Ho, S.: "Learning Symbolic Physics with Graph Networks," 2019, *arXiv:1901.05862v2*.

18. Golmohammadi, A.: "Hybrid Modeling: Challenges and Opportunities in the Subsurface," paper presented at the SPE Workshop: Merging Data-Driven and Physics-Based Models for Enhanced Reservoir Insights and Predictions, San Antonio, Texas, November 19-20, 2019.

19. Sanchez-Gonzalez, A., Godwin, J., Pfaff, T., Ying, R., et al.: "Learning to Simulate Complex Physics with Graph Networks," 2020, *arXiv:2002.09405v2*.

20. Jalving, J, Cao, Y. and Zavala, V.M.: "Graph-Based Modeling and Simulation of Complex Systems," *Computers & Chemical Engineering*, Vol. 125, June 2019, pp. 134-154.

21. Battaglia, P.W., Pascanu, R., Lai, M., Rezende, D., et al.: "Interaction Networks for Learning about Objects, Relations and Physics," paper presented at the 30th Conference on Neural Information Processing Systems, Barcelona, Spain, December 5-10, 2016.

22. Maucec, M., Jalali, R. and Dossary, M.: "Methods and Systems for Generating Graph Neural Networks for Reservoir Grid Models," U.S. Patent Application 2021/0389491 A1, 2021.

23. Sintef: "The 10th SPE Comparative Solution Project, Model 2," 2008, *https://www.sintef.no/projectweb/geoscale/results/msmfem/spe10/*.

24. Dogru, A.H., Fung, L.S.K., Middya, U., Al-Shaalan, T.M., et al.: "New Frontiers in Large-Scale Reservoir Simula-

tion," SPE paper 142297, presented at the SPE Reservoir Simulation Symposium, The Woodlands, Texas, February 21-23, 2011.

25. Equinor: "Equinor/ecl: Software for Reading and Writing the Result Files from the Eclipse Reservoir Simulator," 2021, GitHub repository: *https://github.com/equinor/ecl*.

26. Kingma, D. and Ba, J.: "Adam: A Method for Stochastic Optimization," paper presented at the International Conference on Learning Representations, San Diego, California, May 7-9, 2015.

27. Maucec, M. and Jalali, R.: "Geoscience-Based Deep Interaction Networks for Predicting Flow Dynamics in Reservoir Simulation Models," SPE paper 205952, *SPE Journal*, in press, 2021.

### About the Authors

**Dr. Marko Maucec**

*Ph.D. in Nuclear Engineering, University of Ljubljana*

Dr. Marko Maucec is a Petroleum Engineering Consultant with the Simulation Group of Saudi Aramco's Reservoir Description and Simulation Department. His main responsibilities cover the development and implementation of methods for uncertainty quantification, dynamic model inversion with assisted history matching, production optimization, and data- and physics-driven predictive modeling into reservoir simulation practices.

Marko has been awarded prestigious postdoctoral research tenures, such as the Fulbright and Marie Curie Fellowships, has worked internationally in the nuclear research and industry as well as formerly in the oil industry with Halliburton/Landmark and Shell International E&P.

He has authored more than 80 peer-reviewed and conference papers. Marko is a coauthored on a reference book, *Intelligent Digital Oil and Gas Fields: Concepts, Collaboration, and Right-Time Decisions*, and is an inventor on 30 U.S. patents and patent applications.

He is an active member of the Society of Petroleum Engineers (SPE), a technical peer reviewer for the *SPE Journal*, and a co-organizer of professional events and forums. Marko is an appointed member in the Reservoir Advisory Committee to the Technical Director for SPE's Reservoir technical discipline, and is currently serving as the co-editor for the InTech Open Book Series publication on Applied Spatial-Temporal Data Analytics and Machine Learning.

He received his B.S. degree in Electrical Engineering from the University of Ljubljana, Ljubljana, Slovenia, his M.S. degree in Nuclear Engineering from the University of Maribor, Maribor, Slovenia, and his Ph.D. degree in Nuclear Engineering from the University of Ljubljana, Ljubljana, Slovenia.

Marko completed his postdoctoral work at Claremont Graduate University, Claremont, CA, and the University of Groningen, Groningen, the Netherlands.

**Ridwan S. Jalali**

*M.S. in Computer Science, King Fahd University of Petroleum and Minerals*

Ridwan S. Jalali joined Saudi Aramco in September 2011 as an IT System Analyst. His research areas include data science and machine learning for physical systems, computer vision and cognitive systems, including speech recognition, and natural language understanding.

Ridwan received his B.S. degree in Computer Science from Colorado State University, Fort Collins, CO, and his M.S. degree in Computer Science from King Fahd University of Petroleum and Minerals, Dhahran, Saudi Arabia.

# Imaging Subsurface Targets Using Cross-Borehole GPR: A Field and Modeling Approach

*Jesus M. Felix Servin and Hussain A. Shateeb*

**Abstract /**

Cross-borehole ground penetrating radar (XBGPR) is a geophysical technique that allows for high-resolution characterization of the interwell region. This method relies on the propagation of electromagnetic (EM) waves — typically in the MHz region — that are analyzed to generate subsurface maps of EM properties, which can be interpreted into fluid saturation maps. We present the results of a large-scale field experiment complemented by 3D numerical simulations evaluating the feasibility of locating small fluid targets of different compositions in the subsurface.

An array of 33 target wells and six observation wells completed with nonconductive, nonmagnetic pipe were used to conduct the experiments. The target wells were filled with different fluids, including dielectrically and magnetically tagged fluids, such as polymer solutions and polymer solutions with magnetite. Time-domain EM measurements were acquired using a 100 MHz XBGPR system in a semi-reciprocal tomographic setup. The acquired waveforms were filtered and processed using bh_tomo, an open source platform for XBGPR analysis. Traveltime and amplitude inversions were performed to obtain velocity and attenuation maps of the surveyed area. In parallel, 3D numerical simulations were conducted using a commercially available finite element modeling package. The simulation results were compared and validated with the experimental results.

The simulations are in overall agreement with the field results; showing the right trend in traveltime and amplitude for the different fluids. All fluids caused an increase in traveltime compared to air filled target wells. Water appears to cause the largest increase, followed by AN-132, xanthan, and finally xanthan with magnetite. The observed traveltime is lower than expected. This may be an indication of the wave going around the holes and partially avoiding the slow fluids, especially because the operating wavelength is comparable to the well spacing.

Another possible explanation is that the actual location of the wells is slightly different from the original design due to inaccurate drilling. Yet another possibility is that the array may behave as a periodic structure, causing modal propagation. The attenuation data shows a clear difference between the empty and the liquid filled target holes, but little difference between the liquids. As a whole, the results prove that our approach can be used to locate relatively small fluid targets via EM tomographic surveys with no previous geological information.

Experimental data of XBGPR is rather limited. Our experiments expand the understanding of the challenges and opportunities that such a technique can offer to the oil and gas industry. We have also developed and validated modeling capabilities that will enable improved planning and quick testing of future surveys.

## Introduction

Ground penetrating radar (GPR) is a geophysical technique that allows for high-resolution characterization of the subsurface. GPR uses electromagnetic (EM) propagating waves to probe the subsurface and detect structures and changes in electrical properties via reflection and/or transmission measurements. Comprehensive descriptions of the technique and its applications can be found in the literature[1, 2]. GPR has been used in several fields, such as glacial exploration and monitoring[3, 4], aquifer characterization[5], utility detection[6, 7], mining[8, 9], and voids detection[10], among others.

Signal penetration depends on the operating frequency and propagating media properties, and ranges widely from less than 1 m for clay, to several thousands of meters for ice[11]. Deep investigation is only possible in highly resistive materials and at low operating frequencies (tens of MHz).

GPR surveys can be divided into surface and borehole, depending on the acquisition configuration, and transmission, Fig. 1. Borehole GPR surveys are conducted in reflection mode when only one borehole is available and both the transmitter (Tx) and the receiver (Rx) are sequentially positioned at multiple locations along the same borehole. The reflections, caused by changes in the EM properties of the subsurface, are recorded. When two or

**Fig. 1** *A schematic representation of surface GPR (left), reflection borehole GPR (middle), and transmission borehole GPR (right), also known as cross-borehole GRP.*
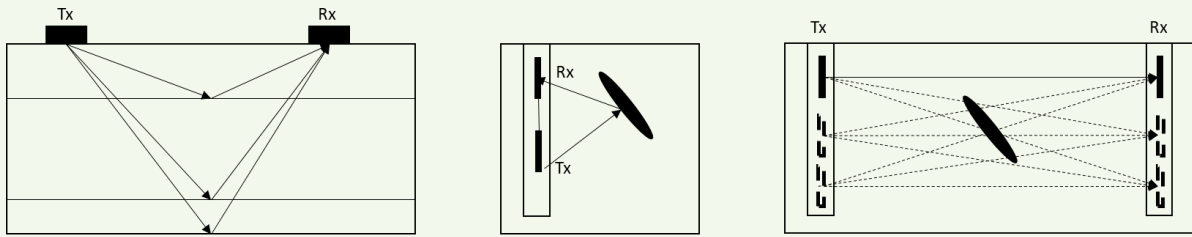


more boreholes are available, the survey can be conducted in transmission mode, also known as cross-borehole GPR (XBGPR).

Our work focuses on XBGPR, in which an EM signal is launched into the medium of interest by a Tx antenna located inside a borehole and the signal is recorded a certain distance away by an Rx antenna located inside a second borehole. Conventionally, the traveltime and first cycle amplitude of the recorded waveforms are picked, Fig. 2, and inverted, to obtain velocity and attenuation maps of the subsurface that can be further interpreted to obtain distribution maps of dielectric permittivity, $\varepsilon$, magnetic permeability, $\mu$, and electric conductivity, $\sigma$. More sophisticated techniques to infer subsurface properties from the received waveforms, such as full waveform inversion, have also been explored and show promising results[5, 12-15].

The operating frequency of most borehole GPR systems is between 20 MHz to 250 MHz, with corresponding wavelengths of 5 m to 0.4 m for common geological materials[13, 16, 17]. Similar to surface GPR, the penetration depth ranges from less than a meter in clay, to tens of meters in crystalline rock, and thousands of meters in salt[11]. XBGPR is less common than surface GPR. Nevertheless, this technique has been implemented in multiple areas, such as mining[9], cavity imaging[17], fracture characterization[18], and hydrogeophysical investigations[19].

The application of borehole GPR in the oil and gas context is rather limited. Subsequently, several studies have been performed in recent years to evaluate the feasibility of incorporating this technique to some of the industry's operations. Zhou (2020)[20] investigated the potential use of this technique for well logging and production monitoring. Heigl et al. (2005)[21] performed simulations to determine if mud invasion can be estimated by means of borehole GPR. Miorali et al. (2011a)[22] and (2011b)[23] proposed a method to monitor water and oil movement in smart wells using permanent downhole GPR systems. Oloumi et al. (2015)[24] investigated the feasibility of imaging oil well perforations using borehole GPR in reflection mode. Chen et al. (2002)[25] showed that this technique is suitable for near wellbore imaging and geosteering applications.

## Theory

In XBGPR, the traveltime and amplitude of the received signals depend on the EM properties of the media through which they propagate. EM waves propagate through air with the speed of light. Consequently, their speed in the subsurface is a function of the EM properties of the subsurface and the frequency of the wave, as described by Eqn. 1:

$$v = \left\{ \sqrt{\mu\epsilon} \sqrt{\frac{1}{2}\left[\sqrt{1 + \left(\frac{\sigma}{\omega\epsilon}\right)^2} + 1\right]} \right\}^{-1} ,$$

(1)

where $v$ is the speed of propagation, $\omega$ is the angular frequency, $\mu$ is the magnetic permeability, $\varepsilon$ is the dielectric permittivity, and $\sigma$ is the electric conductivity. Moreover, if we assume low conductivity (low loss approximation), Eqn. 1 simplifies to Eqn. 2:

$$v = \frac{1}{\sqrt{\mu\epsilon}} .$$

(2)

According to the low loss approximation in Eqn. 2, the speed of propagation is inversely proportional to $\mu$ and $\varepsilon$. Therefore, increasing either $\mu$, or $\varepsilon$, or both, should result in lower propagation speed and increased signal traveltime. Several processes contribute to signal amplitude reduction, including attenuation, spherical spreading, scattering, as well as reflections at the interfaces. Similar to traveltime, attenuation is a function of the EM properties of the propagating medium as well as the signal frequency, as described by Eqn. 3:

**Fig. 2** *A schematic of a received waveform showing the first break, which is used to calculate the traveltime, and the first cycle peak-to-peak amplitude.*

$$\alpha = \omega\sqrt{\mu\epsilon}\sqrt{\frac{1}{2}\left[\sqrt{1+\left(\frac{\sigma}{\omega\epsilon}\right)^2}-1\right]}$$

<div style="text-align:right">3</div>
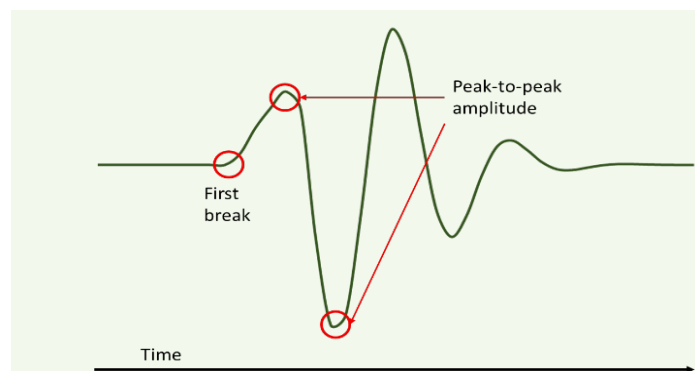
where $a$ is the attenuation constant, $\omega$ is the angular frequency, $\mu$ is the magnetic permeability, $\epsilon$ is the dielectric permittivity, and $\sigma$ is the electric conductivity.

In the case of oil reservoir fluids, significant changes in $\sigma$ and $\epsilon$ are typically observed between oil and brine. Moreover, changes in $\mu$ are not usually observed, unless magnetic materials, such as iron oxide, are present in the formation. Therefore, $\mu$ may serve as a contrast to label injected fluids such that they can be differentiated from the fluids already present in the reservoir.

The purpose of this work is to investigate the feasibility of labeling fluids using magnetic and dielectric contrast agents, and locating them via XBGPR surveys. A series of large-scale experiments performed using an array of shallow wells are presented.

## Testing Platform

An array of shallow wells designed to function as a testing platform for novel EM approaches was used to conduct the experiments. The entire platform consists of 47 wells of different depths and diameters, completed with non-conductive and nonmagnetic casing to be suitable for EM transmissions, Fig. 3. All wells were sealed from the bottom so that no fluids can leak from or into the wellbores. Depending upon the inner diameter, depth, and location, the wells are divided in four categories: deep observation wells (DO1 to DO2), far observation wells (O1 to O6), near observation wells (O7 to O12), and shallow wells (C1-1 to C3-11). Table 1 summarizes

the specifications and number of wells drilled for each category. For this work, only the near observation and shallow wells were used, the other wells are reserved for future tests.

The array design takes into consideration important parameters to improve the quality of the planned EM surveys. In the case of XBGPR, the borehole depth, $D$, to borehole separation, $S$, as a rule of thumb should be greater than 2. Meeting this condition maximizes the angle coverage and prevents refracted airwaves from masking direct arrivals[2]. At the same time, it is important to make sure that $S$ is large enough to be in the far field of the antenna radiation, such that Eqn. 4 is met:

$$S > \frac{v}{f}$$

<div style="text-align:right">4</div>

where $v$ is the ground velocity and $f$ is the GPR center frequency.

In our case, the borehole depth is 40 m, and the borehole

**Table 1** A summary of wells drilled and their dimensions.

| Type of Well | Inner Diameter (m) | Depth (m) | # of Wells |
|---|---|---|---|
| Deep observation | 0.3048 | 200 | 2 |
| Far observation | 0.3048 | 40 | 6 |
| Near observation | 0.1524 | 40 | 6 |
| Shallow wells | 0.3048 | 30 | 33 |

**Fig. 3** A schematic representation of the testing platform. For the experiments presented in this work, only Wells O7-O12 and C1-1 to C3-11 were used.
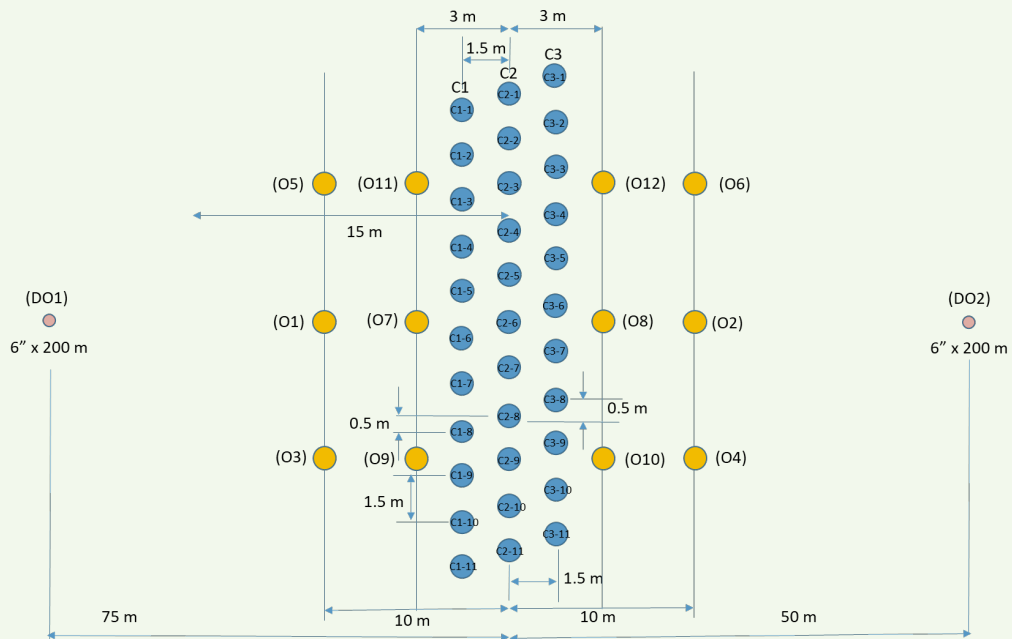
separation is 6 m, yielding a ratio of 6.67, well above the minimum recommendation of 2. The borehole separation is also larger than the velocity to center frequency ratio, which is approximately 1.2. Therefore, the dimensions of our array ensure significant angle coverage and far field conditions for the measurements.

## Acquisition System and Procedure

A typical XBGPR system consists of three main components: a control unit, a power supply system, and antennas. For our tests, we used a pair of MALA Borehole 100 MHz Slimhole Antennas coupled to a MALA ProEx control unit. The antennas are powered downhole by batteries, and the data is conveyed to the control unit at the surface via fiber optics to avoid EM interference.

The data was collected in a tomographic manner between pairs of observation wells using a multiple offset gathers approach. To maintain a balance between the time required to conduct each survey and the ray coverage, we opted for a semi-reciprocal acquisition setup, Fig. 4. This approach yields higher resolution in the center and lower resolution close to the wellbore. It also yields higher ray coverage than a sparse setup and it is less time-consuming than a dense setup[16].

Prior to lowering the antennas, the traveltime through

**Fig. 4** *A schematic of the three different acquisition setups. Sparse (left) results in ray coverage gaps close to the wellbore, semi-reciprocal (middle) improves ray coverage near to the wellbore, dense (right) results in the best ray coverage, but at increased data size and acquisition effort.*



air for a known distance was recorded, to be used as a time-zero correction. Next, the Tx was lowered 5 m below the surface and the Rx was moved from 5 m above the Tx, to 5 m below it, collecting waveforms every 0.1 m. It has been reported that when the angle between the Tx and Rx is large, the signal is received away from the antenna feed points, leading to errors in velocity estimates[26]. Consequently, we limited the acquisition to 5 m above and below the position of the Tx, which limits the angle to no more than 40°. Then, the Tx was lowered 1 m and the acquisition from 5 m above to 5 m below it every 0.1 m was repeated.

This process continued until the Tx reached a depth of 35 m. Next, both tools were brought to the surface and a second time-zero correction shot was acquired. We then exchanged the Tx and Rx boreholes and repeated the acquisition process previously described. This procedure was repeated for each pair of wells.

## Experiments and Fluid Preparation

The experiments involved filling the shallow wells with a certain type of fluid and conducting XBGPR tomographic acquisitions using the near observation wells. Five different experiments were conducted based on the type of fluid filling the shallow boreholes. Table 2 summarizes the composition of each fluid, as well as the approximate EM properties. The well water was obtained from a well in the vicinity of the testing area. The AN-132 polymer was acquired from SNF; the xanthan gum had a technical grade purity level and was acquired from FuFeng; the magnetite was acquired from LKAB under the commercial name of MagnaChem10. All chemicals were used as received.

Mixing for fluids 3 to 5 was performed in a large tank with three rotating blades mounted at the top. The mixing procedure consisted of first filling the tank with water to 80% to 90% of the desired volume. Then, adding the magnetite (if applicable), followed by the polymer (xanthan or AN-132), while mixing. Next, mixing was stopped and the tank was topped up to the final volume. Finally, mixing was resumed and continued for one hour. During that time, the viscosity of the fluid was monitored. Approximately three batches had to be prepared for each experiment. Overall, the fluids looked homogeneous and the viscosity between different batches was comparable.
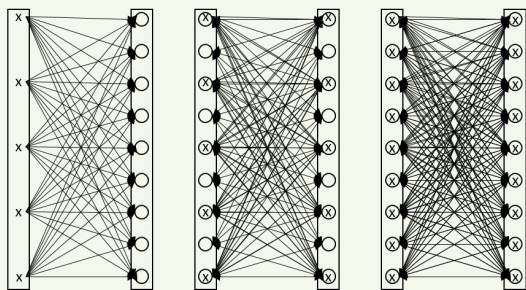
**Table 2** *The fluids used to fill the shallow wells for each of the performed experiments.*

| # | Name | Fluid | σ [S/m] | $\varepsilon_r$ | $\mu_r$ |
|---|------|-------|---------|------|------|
| 1 | Air (baseline) | Air | ~0 | 1 | 1 |
| 2 | Water | Well water | 0.5 | 80 | 1 |
| 3 | AN-132 | 2.5 g/L of AN-132 dissolved in well water | 0.7 | > 80 | 1 |
| 4 | Xanthan | 5.0 g/L of xanthan dissolved in well water | 0.8 | > 80 | 1 |
| 5 | Magnetite | 7.5 g/L of xanthan and 100 g/L of magnetite dissolved in well water | 1.0 | > 80 | > 1 |

## Data Processing Workflow

Data processing and interpretation was done using bh_tomo[27], an open-source platform developed for GPR surveys. The raw data was subjected to the following preprocessing workflow:

1. Filtering: A band pass filter was used to remove noise from the data. The low and high cut frequencies used are 10 MHz and 250 MHz, respectively.

2. Pruning: Stations shallower than 5 m below the surface were removed, to avoid refracted waves propagating through the air. In addition, waveforms with a signal-to-noise ratio (SNR) below 1 were pruned. This process generally removed 30% to 50% of the data.

After filtering and pruning, the data was processed to pick the traveltime and peak-to-peak amplitude for each trace.

## Traveltime Analysis

Traveltime picking was done using the semi-automatic traveltime picking module of bh_tomo. This approach entails picking the first break of a series of waveforms that are used to automatically pick the first break of the remaining data using cross correlation. Next, the manual traveltime picking module was used to quickly browse through the picked times and correct obvious mistakes. Most of the errors were due to low SNR. Once the data were picked, we proceeded to compare the traveltimes for different fluids.

### Traveltime Difference

The traveltime difference was estimated by comparing the picked traveltime for a given Tx-Rx position for different fluids. This information was used as a first approximation to evaluate if the fluids were having an impact on the signal's traveltime. This may be the best way to see small changes, because traveltime inversion involves smoothing, which could mask small changes in slowness.

Figure 5 shows the traveltime difference between water and air for well pairs O7 and O12. Most of the differences are positive, meaning that the traveltime is longer when the wells are filled with water than when they are filled with air. It should be noted that the traveltime difference is generally small (< 4 ns). Similar results were obtained when comparing AN-132 and magnetite with air (data not shown).

### Traveltime Inversion

The next step involved inverting the traveltime data to obtain a map of slowness. Multiple grid element sizes for the inversion models were tested. The best results were obtained using elements of 0.25 m by 0.25 m, where the bh_tomo offers two different algorithms to perform the inversion, geostatistics and LSQR. For the work presented here, only the latter was used. Table 3 summarizes the parameters used to perform the inversion. In the absence of other constraints, the smoothing weight in x and z were modified until a minimum in the variance of the residuals ($\sigma^2$) was obtained, Fig. 6. The inversion generates a map of subsurface velocity between two wells, Fig. 7.

In addition to the regular inversion, bh_tomo has two options that allow for time-lapse evaluation of the data. The first one is simultaneous inversion, in which two data sets are inverted simultaneously while trying to be

**Table 3** *The parameters used to perform the traveltime inversion using the LSQR algorithm.*

| Parameter | Value |
| --- | --- |
| Number of straight rays' iterations | 1 |
| Number of curved rays' iterations | 2 |
| Solver tolerance | 1e-6 |
| Maximum number of solver iterations | 100 |
| Constraints weights | 1 |
| Smoothing weight x | 10 |
| Smoothing weight y | 10 |
| Smoothing weight in z | 10 |
| Smoothing operator order | 2 |
| Maximum model parameter variation per iteration | 50% |

**Fig. 5** *The traveltime difference between water and air for Wells O7 and O12. Since most of the traveltime differences are positive, it can be concluded that overall water is slower than air.*
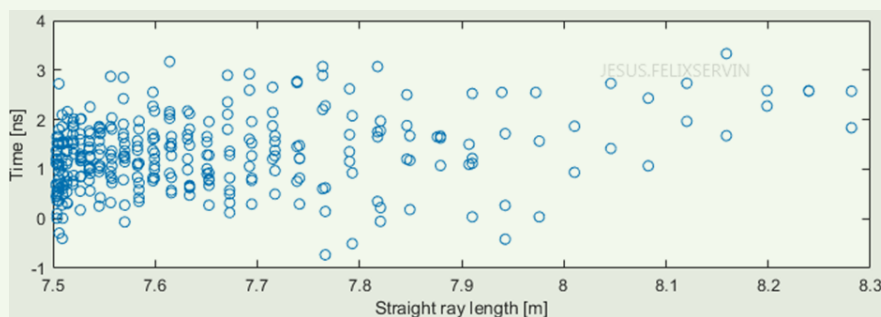
**Fig. 6** *The norm of the residuals (top left), residuals histogram (bottom left), residuals as a function of angle with respect to the horizontal (top right) and residuals as a function of Tx and Rx depth (bottom right). The smoothing weights was changed until a minimum in the variance of the residuals was achieved.*
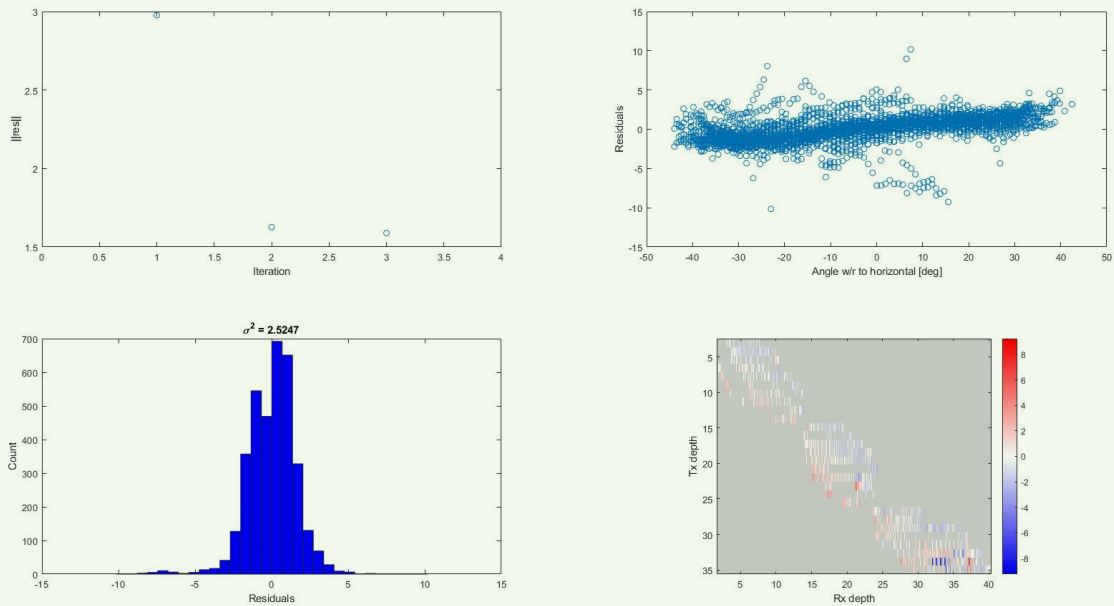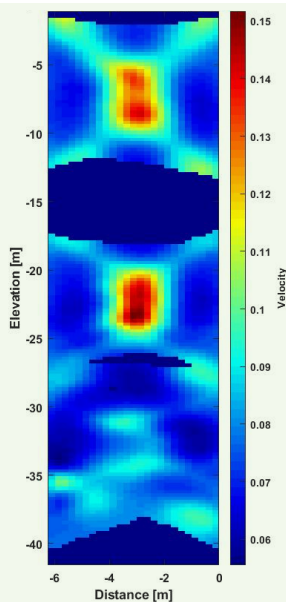


**Fig. 7** *The velocity map obtained for the two well panels (O12-O11 and O11-O12) inverted together with air-filled shallow wells. The fast regions are present in the center of the map, corresponding to the location of the shallow wells.*



on inverting the change in traveltime difference rather than the traveltime itself. Both approaches were tested but simultaneous inversion did not generate satisfactory results. We speculate that the differences were too small and were masked by this approach. The second approach is better suited for small changes in traveltime. Subsequently, one limitation is that it assumes the ray paths are the same for both data sets. This assumption is reasonable if the difference in traveltime is small; however, it may not be suitable in situations where the difference in traveltime is large or if the soil conditions significantly changed from one survey to the other. The result of the inversion is a map of percentage change in slowness, Fig. 8. Regions where the change is positive represent portions of the reservoir that became slower in the second survey.

### Amplitude Analysis and Inversion

Peak-to-peak amplitude picking was performed using the automatic function provided by bh_tomo. Next, the traces were inspected manually to correct obvious mistakes. Amplitude inversion was done using the LSQR algorithm to obtain maps of attenuation. The fitting parameters are the same used for the traveltime inversion, Table 3, and were optimized to minimize the variance of the residuals. The inversion generates a map of attenuation between two wells, Fig. 9.

## Results and Discussion

A subset of six panels corresponding to well pairs O8-O9, O12-O7, and O12-O11 were used to evaluate the results. We begin by investigating the data quality and ray coverage. The data shows low ray coverage in some regions and a complete lack of data for certain intervals,

as close as possible to a reference tomogram; for example, air and water, with air as the reference. In this case, the simultaneous inversion would highlight the differences caused by the water. The second approach consists

**Fig. 8**  *A map of change in slowness, as a percentage, obtained for Wells O8-O9 and O9-O8 traveltime values of water minus air and using the inversion of air as the reference. Increases in slowness are shown in the central region, where the wells are located. This means that water is causing those regions to become slower than when the wells were empty.*
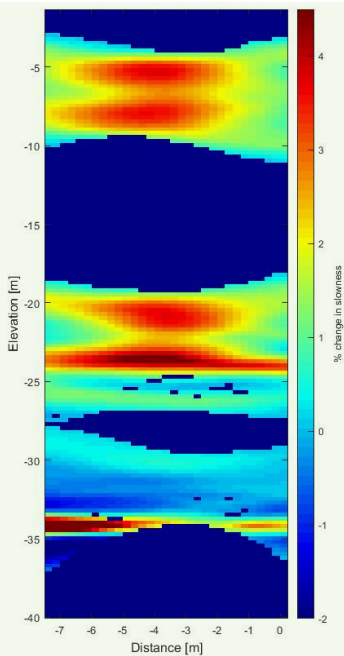


**Fig. 9**  *An attenuation map obtained for well panels O8-O9 and O9-O8 inverted together with magnetite filled shallow wells. High attenuation regions are present in the center of the map, corresponding to the location of the shallow wells.*
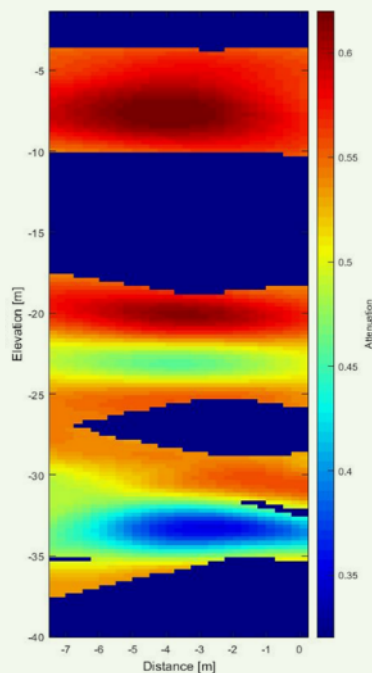
Fig. 10. Based on the resistivity logs of DO1 and DO2, it appears that for values below 50 $\Omega$m, the signal falls below the limit of detection before reaching the Rx. We speculate that these intervals correspond to layers of clay, which are known to result in high attenuation for GPR signals[11]. Based on the ray coverage, we conclude that large variations in resistivity are present within the array. For example, for well pair O12-O7 there is no ray coverage below 25 m, while there is significant coverage for the other two well pairs, especially O12-O11. This suggests that some of the layers may not be continuous across the entire array. Because of the lack of data, the results obtained from regions with low ray coverage will have higher uncertainty.

The traveltime difference data suggests that filling the wells with liquids results in increased traveltime. Figure 11 shows the traveltime difference between water and air (top) and magnetite and water (bottom) for the panels obtained from Wells O7 and O12. Most of the traveltime differences for the first case are positive, meaning that filling the shallow wells with water increases the signal's traveltime.

A similar trend is observed when the wells are filled with fluids 3 to 5. This trend was expected because all liquids have higher $\varepsilon$ and/or $\mu$ than water, but it must be noted that the traveltime is shorter than anticipated. This may be an indication of the wave going around the wells and partially avoiding the slow fluids, especially because the operating wavelength is comparable to the well spacing. Another factor that may contribute to this discrepancy is that the actual location of the wells is different from the original design due to inaccuracy while drilling.

Consequently, in some cases, only a small portion of a fluid filled well is between the observation wells, rather than the entire well. When we compare magnetite and water, we observe that most of the traveltime differences are negative. This suggests that magnetite reduces the signal travel as compared to just water. A similar trend is observed when fluids 3 and 4 are compared with water. This trend was not expected because the product of $\varepsilon$ and $\mu$ for fluids 3 to 5 should be higher than for water. Therefore, an increase on signal traveltime for these fluids over water was expected.

The inversion of the traveltime difference shows similar results: an increase in slowness when the shallow wells are filled with liquids, Fig. 12, water showing the greatest increase, followed by AN-132, xanthan, and finally magnetite. Based on the estimated EM properties of the fluids, Table 2, we expected water to result in the shortest traveltime and magnetite in the longest; however, the data shows the opposite.

The attenuation data shows a clear difference between air filled and liquid filled shallow wells, but similar attenuation among the different liquids, with AN-132 showing the lowest attenuation, followed by xanthan, and then water and magnetite, Fig. 13. As expected, filling the wells with conductive liquids increases the signal attenuation.

To understand the potential reasons for the discrepancies observed in the traveltime data, 3D numerical

**Fig. 10** *From left to right, the resistivity log for DO2, ray coverage for well panel O9-O8, ray coverage for well panel O12-O7, ray coverage for well panel O12-O11, and the resistivity log for well panel DO1. The intervals of low or null ray coverage seem to correlate with regions where the resistivity is below 50 Ωm.*
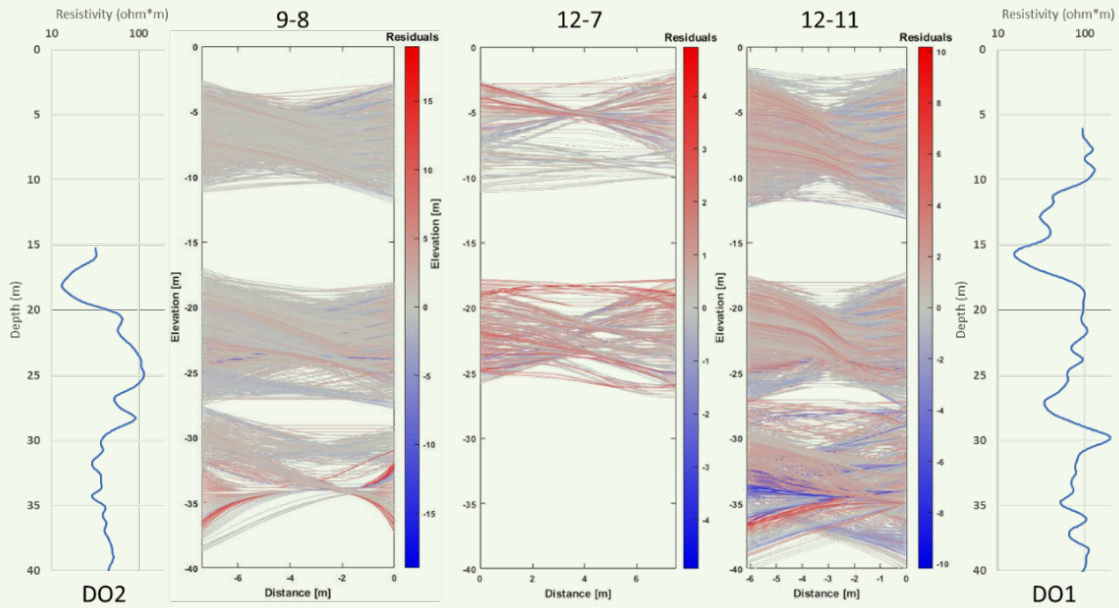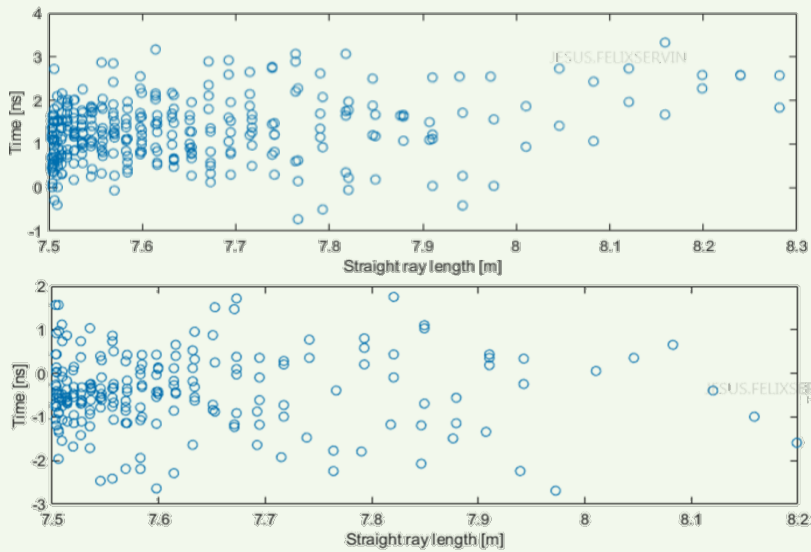


**Fig. 11** *The traveltime difference between water and air (top), and magnetite and water (bottom) for Wells O7 and O12.*



simulations that employed parameters similar to those encountered in the field were conducted using a commercially available finite element package. The numerical model was developed using a strategy similar to the one presented by Felix Servin et al. (2019)[28]. The simulation results confirm our experimental results: water appears to be the slowest fluid, followed by xanthan and then magnetite, Fig. 14.

This trend was not anticipated based on the EM properties of the fluids. We speculate that a likely explanation for such unexpected behavior is that the array is acting as a periodic structure imposing constraints on the propagation mode of the wave, leading to nonmonotonic relationships between the phase speed and the EM properties. Overall, the simulations agree with the experimental results; not only showing that the liquids are slower than air, but also displaying the right trend for the traveltime: water being the slowest, followed by

**Fig. 12**  *Maps of change in slowness. From left to right, water minus air, AN-132 minus air, xanthan minus air, and magnetite minus air. From top to bottom, well panel 8-9, well panel 12-7, and well panel 12-11.*
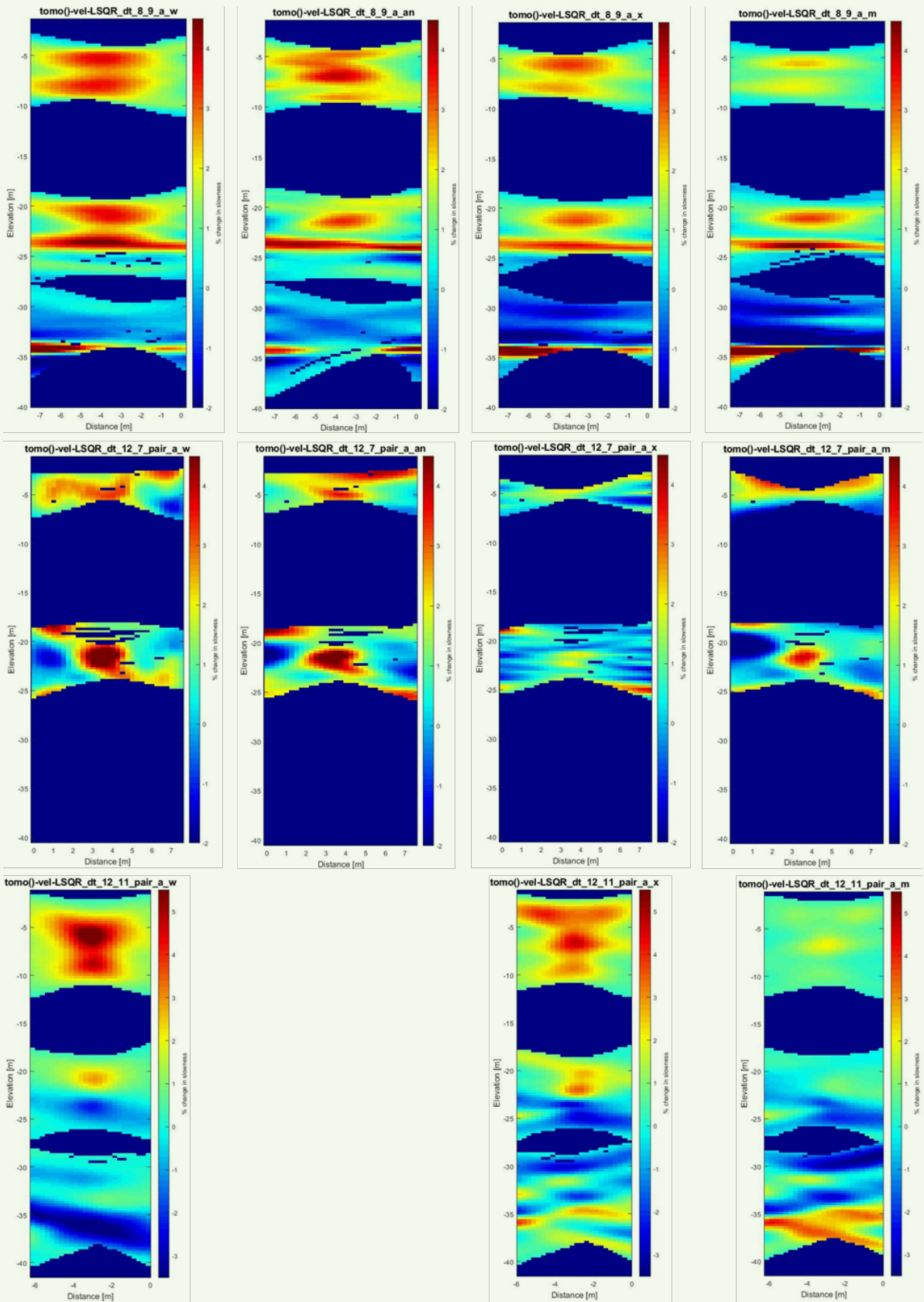
**Fig. 13** *From left to right, maps of attenuation for well pair O8-O9 when filled with air, water, AN-132, xanthan, and magnetite, respectively.*
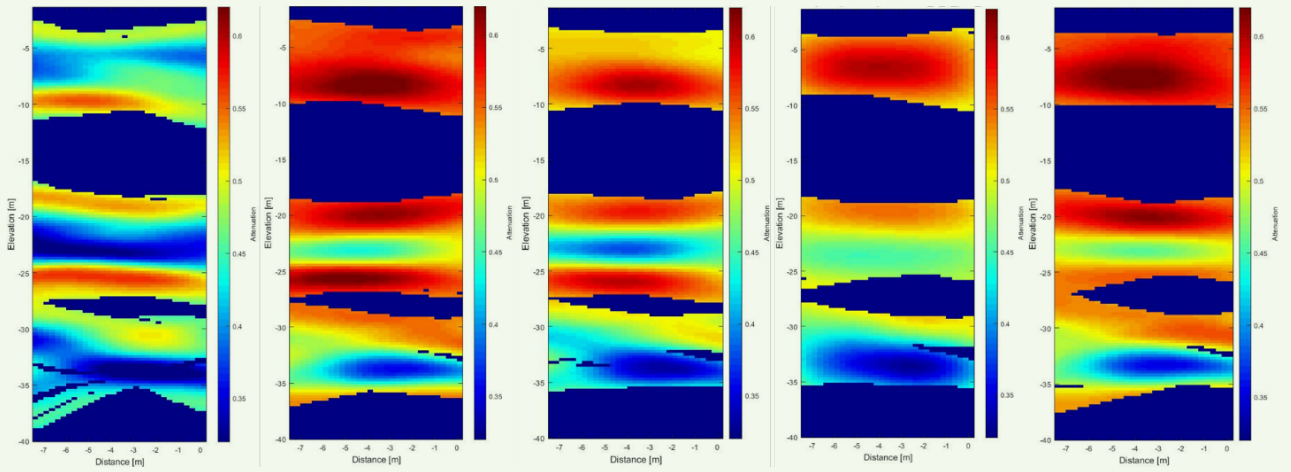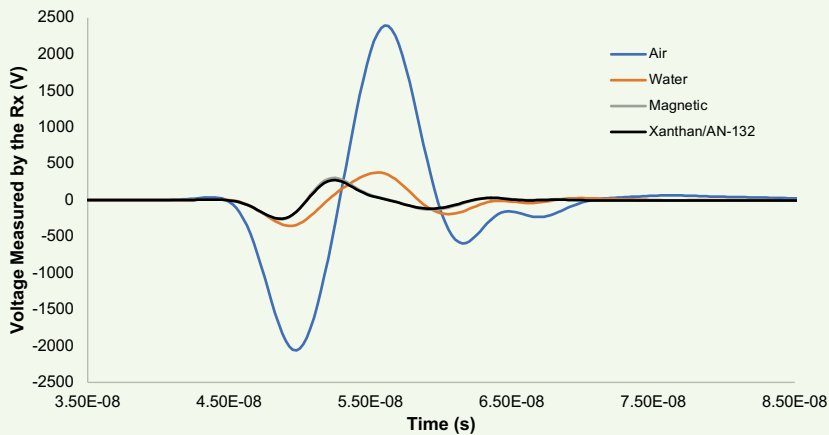


**Fig. 14** *The simulated received waveforms for different fluids for a 100 MHz signal.*



AN-132, xanthan, and then magnetite. Based on the simulations, the difference in traveltime between water, AN-132, and xanthan is likely due to the difference in $\sigma$. Moreover, the difference in traveltime is observed not on the first arrival, but on the second peak of the signals.

The implications are that the inversion algorithm may have to be modified to account for this. It is also shown that increasing $\sigma$ reduces traveltime, e.g., water vs. xanthan. This confirms our hypothesis that fluids that are more conductive will prevent the signal from penetrating deep into the wellbore, and therefore will diminish the effect of the fluids on the signal's traveltime.

The simulations also show that while water should result in reduced attenuation, the rest of the liquids should have similar amplitude. The field results show water resulting in attenuation comparable to the other fluids. This could be a consequence of slight changes in the saturation of the matrix due to rain in the days leading

to some of the experiments; however, the results are in overall agreement with the simulations.

## Conclusions

The results of these tests prove that XBGPR surveys can be used to locate relatively small targets of fluids via time-lapse tomographic surveys, even with no previous geological information. We were able to demonstrate the effect of $\mu$ and/or $\sigma$ on the signal traveltime and amplitude. Consequently, the traveltime effect is smaller and the trend is different from what was originally anticipated, most likely due to the periodic structure of the array and the difference in $\sigma$ of the fluids. The observed trends concur with the 3D numerical simulations, highlighting the importance of conducting simulations before and after future tests.

An analysis of the traveltime data enables differentiating between air and liquid targets, and to a lesser degree one

liquid from another. Subsequently, the behavior is not what was expected prior to conducting the experiments. Based on the experimental and simulations results, we conclude that the electrical conductivity of the fluids has a significant effect on traveltime. For a given fluid, increasing the conductivity will reduce the traveltime. Looking at the attenuation data, we conclude that increasing conductivity will also reduce signal amplitude.

Because of the difference in conductivity between the different fluids, it was not possible to quantify how much effect $\mu$ had on signal traveltime. Future tests should be designed such that all fluids have as much as possible the same conductivity. Due to the design of the testing platform, sharp changes in EM properties are expected between the rock and the wells. Consequently, inversion involves smoothing, and therefore, is not best suited for sharp changes. It may be worth exploring the possibility of using full waveform inversion. It must also be noted that in the reservoir, such sharp changes are not expected.

Moving forward, we recommend conducting similar experiments in reflection mode, since this setup appears to be more suitable for oil and gas applications, given the rather limited penetration obtained in transmission mode.

## Acknowledgments

## References
1. Annan, A.P.: "GPR — History, Trends, and Future Developments," *Subsurface Sensing Technologies and Applications*, Vol. 3, October 2002, pp. 253-270.

2. Annan, A.P.: "Ground-Penetrating Radar," Chapter 11 in *Investigations in Geophysics*, Butler, D.K. (ed.), Society of Exploration Geophysicists, 2005, 758 p.

3. Sun, B., Siegert, M.J., Mudd, S.M., Sugden, D., et al.: "The Gamburtsev Mountains and the Origin and Early Evolution of the Antarctic Ice Sheet," *Nature*, Vol. 459, June 2009, pp. 690-693.

4. Lamsters, K., Karušs, J., Rečs, A. and Bērziņš, D.: "Detailed Subglacial Topography and Drumlins at the Marginal Zone of Mulajokull Outlet Glacier, Central Iceland: Evidence from Low Frequency GPR Data," *Polar Science*, Vol. 10, December 2016, pp. 470-475.

5. Klotzsche, A., van der Kruk, J., Meles, G.A., Doetsch, J.A., et al.: "Full Waveform Inversion of Crosshole Ground Penetrating Radar Data to Characterize a Gravel Aquifer Close to the River Thur, Switzerland," *Near Surface Geophysics*, Vol. 8, Issue 6, June 2010, pp. 635-649.

6. Prego Martinez, F.J., Solla, M., Puente, I. and Arias, P.: "Efficient GPR Data Acquisition to Detect Underground Pipes," *NDT & E International*, Vol. 91, June 2017, pp. 22-31.

7. Šarlah, N., Podobnikar, T., Ambrožič, T. and Mušič, B.: "Application of Kinematic GPR-TPS Model with High 3D Georeference Accuracy for Underground Utility Infrastructure Mapping: A Case Study from Urban Sites in Celje, Slovenia," *Remote Sensing*, Vol. 12, Issue 8, April 2020.

8. Cook, J.C.: "Radar Exploration Through Rock in Advance of Mining," *Transactions of the Society Mining Engineers*, Vol. 254, 1976, pp. 140-146.

9. Fullagar, P.K., Livelybrooks, D.W., Zhang, P., Calvert, A.J., et al.: "Radio Tomography and Borehole Radar Delineation of the McConnell Nickel Sulfide Deposit, Sudbury, Ontario, Canada," *Geophysics*, Vol. 65, Issue 6, November 2000, pp. 1920-1930.

10. Rodeick, C.A.: "Roadbed Void Detection by Ground Penetrating Radar," *Highway & Heavy Construction*, Vol. 127, 1984, pp. 60-61.

11. Slob, E., Sato, M. and Olhoeft, G.: "Surface and Borehole Ground Penetrating Radar Developments," *Geophysics*, Vol. 75, Issue 5, September 2010, pp. 75A103-75A120.

12. Klotzsche, A., van der Kruk, J., Vereecken, H., Meles, G.A., et al.: "High Resolution Imaging of the Unsaturated and Saturated Zones of a Gravel Aquifer Using Full Waveform Inversion," paper presented at the 6th International Workshop on Advanced Ground Penetrating Radar, Aachen, Germany, June 22-24, 2011.

13. Klotzsche, A., van der Kruk, J., Meles, G.A. and Vereecken, H.: "Crosshole GPR Full Waveform Inversion of Waveguides Acting as Preferential Flow Paths within Aquifer Systems," *Geophysics*, Vol. 77, Issue 4, July 2012, pp. H57-H62.

14. Klotzsche, A., van der Kruk, J., Linde, N., Doetsch, J., et al.: "3-D Characterization of High Permeability Zones in a Gravel Aquifer Using 2-D Crosshole GPR Full Waveform Inversion and Waveguide Detection," *Geophysical Journal International*, Vol. 195, Issue 2, November 2013, pp. 932-944.

15. Yang, X., Klotzsche, A., van der Kruk, J., Vereecken, H., et al.: "Full-Waveform Inversion of Cross-Hole GPR Data Measured at the Boise Gravel Aquifer," paper presented at the 6th International Workshop on Advanced Ground Penetrating Radar, Aachen, Germany, June 22-24, 2011.

16. Klotzsche, A.: "Full-Waveform Inversion of Crosshole GPR Data for Hydrogeological Applications," Forschungszentrum Jülich, Zentralbibliothek, 2013.

17. Tronicke, J. and Hamann, G.: "Vertical Radar Profiling: Combined Analysis of Traveltimes, Amplitudes, and Reflections," *Geophysics*, Vol. 79, Issue 4, July 2014, pp. H23-H35.

18. Zhou, H., and Sato, M.: "Subsurface Cavity Imaging by Crosshole Borehole Radar Measurements," *IEEE Transactions on Geoscience and Remote Sensing*, Vol. 42, Issue 2, February 2004, pp. 335-341.

19. Jang, H., Kuroda, S. and Kim, H.J.: "Efficient Electromagnetic Imaging of an Artificial Infiltration Process in the Vadose Zone Using Cross-Borehole Radar," *IEEE Geoscience and Remote Sensing Letters*, Vol. 8, March 2011, pp. 243-247.

20. Zhou, F.: "Novel Applications of Ground Penetrating Radar in Oil Fields," Ph.D. thesis, Delft University of Technology, 2020.

21. Heigl, W.M. and Peeters, M.: "Can We Obtain Invasion Depth with Directional Borehole Radar?" *Petrophysics*, Vol. 46, Issue 1, January 2005, pp. 52-61.

22. Miorali, M., Slob, E. and Arts, R.: "A Feasibility Study of Borehole Radar as a Permanent Downhole Sensor," *Geophysical Prospecting*, Vol. 59, Issue 1, January 2011, pp. 120-131.

23. Miorali, M., Zhou, F., Slob, E. and Arts, R.: "Coupling Ground Penetrating Radar and Fluid Flow Modeling for Oil Field Monitoring Applications," *Geophysics*, Vol. 76, Issue 3, May 2011, pp. A21-A25.

24. Oloumi, D., Pettersson, M.I., Mousavi, P. and Rambabu, K.: "Imaging of Oil Well Perforations Using UWB Synthetic Aperture Radar," *IEEE Transactions on Geoscience and Remote Sensing*, Vol. 53, Issue 8, February 2015, pp. 4510-4520.

25. Chen, Y-H. and Oristaglio, M.L.: "A Modeling Study of Borehole Radar for Oil Field Applications," *Geophysics*, Vol. 67, Issue 5, September 2002, pp. 1486-1494.

26. Irving, J.D. and Knight, R.J.: "Effect of Antennas on Velocity Estimates Obtained from Crosshole GPR Data," *Geophysics*, Vol. 70, Issue 5, September 2005, pp. K39-K42.

27. Giroux, B., Gloaguen, E. and Chouteau, M.: "bh_tomo — a Matlab Borehole Georadar 2D Tomography Package," *Computers & Geosciences*, Vol. 33, Issue 1, January 2007, pp. 126-137.

28. Felix Servin, J.M., Deffenbaugh, M., Adams, R. and Riachentsev, V.: "Can we Propagate MHz EM Signals for 1 km through the Subsurface in the Presence of Conductive Media?" *SEG Technical Program Expanded Abstracts 2019*, pp. 1164-1168.

*About the Authors*

**Jesus M. Felix Servin**

*M.S. in Chemical and Biological Engineering, King Abdullah University of Science and Technology*

Jesus M. Felix Servin joined the Reservoir Engineering Technology Division of Saudi Aramco's Exploration and Petroleum Engineering Center – Advanced Research Center (EXPEC ARC) in February 2012. His focus is on the development of electromagnetic methods and nanoparticle-based contrast agents for reservoir characterization and monitoring. Jesus's role has been instrumental in the development and deployment of the Magnetic Nano-Mappers project, including hardware design and in-house fabrication, instrumentation, computer programming, and

data processing.

Jesus' interests include the development of nanoscale strategies for reservoir illumination and electromagnetic methods for reservoir description and monitoring.

He received his B.S. degree in Engineering Physics from Instituto Tecnologico y de Estudios Superiores de Monterrey, Monterrey, Mexico, and an M.S. degree in Chemical and Biological Engineering from King Abdullah University of Science and Technology, Thuwal, Saudi Arabia.

**Hussain A. Shateeb**

*A.S. in Industrial Chemistry Technology, Jubail Industrial College*

Hussain A. Shateeb joined Saudi Aramco as an Apprentice Technician in the Vocational College Graduates (VCGNE) Training Program in August 2014. Upon attaining his degree in 2016, he then then joined the Reservoir Engineering Technology Division of Saudi Aramco's Exploration and

Petroleum Engineering Center – Advanced Research Center (EXPEC ARC), where he works as a Lab Technician.

Hussain received his A.S. degree in Industrial Chemistry Technology from Jubail Industrial College, Jubail, Saudi Arabia.